Du and Audétat; Early sulfide saturation is not detrimental to porphyry Cu-Au formation.

SUPPLEMENTARY MATERIAL

CONTENTS

1. Supplementary text

1.1. Analytical methods

For each sample listed in Table 1, polished thick sections of 100 to 150 µm thickness were prepared and examined with a standard petrographic microscope. Special attention was paid to the occurrence of sulfide inclusions and crystallized silicate melt inclusions, as they provide information on the composition of silicate melts and coexisting sulfide phases.

LA-ICP-MS

Unexposed silicate melt inclusions, sulfide inclusions, and their host minerals were analyzed by laser-ablation inductively-coupled-plasma mass-spectrometry (LA-ICP-MS) at the Bavarian Geoinstitute, University of Bayreuth. The utilized system consists of a 193 nm ArF Excimer laser (GeoLasPro system, Coherent, USA) attached to a quadrupole mass spectrometer (Elan DRC-e, Perkin Elmer, Canada). The sample chamber was flushed with He gas at a rate of 0.4 l/min, to which 5 ml/min H_2 gas was added on the way to the ICP-MS. Analyzed isotopes include ^{11}B, ^{23}Na, ^{25}Mg, ^{27}Al, ^{30}Si, ^{31}P, ^{32}S, ^{35}Cl, ^{39}K, ^{43}Ca, ^{49}Ti, ^{51}V, ^{53}Cr, ^{55}Mn, ^{57}Fe, ^{59}Co, ^{62}Ni, ^{65}Cu, ^{66}Zn, ^{75}As, ^{82}Se, ^{85}Rb, ^{88}Sr, ^{89}Y, ^{90}Zr, ^{93}Nb, ^{98}Mo, ^{105}Pd, ^{107}Ag, ^{111}Cd, ^{125}Te, ^{133}Cs, ^{137}Ba, ^{139}La, ^{140}Ce, ^{181}Ta, ^{195}Pt, ^{197}Au, ^{205}Tl, ^{208}Pb, ^{209}Bi, ^{232}Th and ^{238}U, using dwell times of 10 to 50 ms per isotope. The laser was operated at 5 to 10 Hz and an energy density of 3 to 10 J/cm^2 on the sample surface, using laser pits ranging from 10 to 80 µm in diameter. The ICP-MS system was tuned to a ThO rate of 0.07 ± 0.02 % and a rate of doubly charged Ca ions of 0.25±0.05 % based on analyses of NIST SRM 610 glass. Silicate minerals were quantified using NIST SRM 610 glass as external standard and then normalizing the sum of all major element oxides to 100 wt % in the case of clinopyroxene, to 98 wt % in the case of phlogopite, and to 97 wt % in the case of amphibole.

Entire, unexposed melt inclusions were drilled out of the clinopyroxene host, and excess ablated host was subtracted numerically from the resulting LA-ICP-MS signals until the constraint for the internal standard was matched (Halter et al. 2004; Pettke 2006). External standardization was based on NIST SRM 610 glass (Jochum et al. 2011). Internal standardization was based on the SiO_2 vs. CaO trend displayed by whole-rock data (Wang et al., 2003, 2015, 2016; Huang et al., 2004; Yan et al., 2008; Xie et al., 2012 a, b; Guo et al., 2013; Li et al., 2014; Chen et al., 2016; Du et al., 2018). The sum of all major element oxides was normalized to 100 wt%. Sulfur and Cl abundances were quantified using the approach described in Rottier and Audétat (2019), which involves a well-characterized afghanite crystal as external standard and two correction equations: (i) one for the amount of excess S signal produced by the ablation of S-free materials, and (ii) one to account for the remaining discrepancy during analyses of S-bearing materials. Both correction equations were renewed at the day of the melt inclusion analysis.

In the case of the sulfide inclusions, host was numerically subtracting until no Al_2O_3 was left. External standardization was based on a synthetic pyrrhotite (Po724 T3 SRM of the Memorial University of Newfoundland) to constrain the Fe/S ratio, whereas NIST SRM 610 was used to constrain the ratio of Fe to all other elements. Internal standardization was

performed by normalizing the sum of S, Fe, Co, Ni and Cu to 100 wt%. Zhang and Audétat (2017a) demonstrated that this approach provides accurate results for various Fe-Cu-S minerals and a synthetic, trace element-doped monosulfide solid solution (MSS) reference material described in Brenan (2015). A simple equation was used to correct measured ^{105}Pd concentrations for an interference caused by $^{65}Cu^{40}Ar$ (Chang and Audétat, 2018). Unexposed Fe-Ti-oxide inclusions were quantified by numerically subtracting host until no SiO_2 was left. Element concentration ratios were quantified based NIST SRM 610 and then normalized to 100 wt%.
Uncertainties associated with the LA-ICP-MS analyses of silicate minerals, oxide minerals and sulfide inclusions are ≤ 5-8 % (Zhang and Audétat, 2017a; Chang and Audétat, 2018), except for elements close to the detection limit. For the silicate melt inclusions the uncertainties are considerably higher (10-20 %) because the host correction is sensitive to minor variations in mineral composition and potential diffusional re-equilibrations (e.g. Danyushevsky et al. 2000).

Electron microprobe analysis
Electron microprobe analysis on clinopyroxene, amphibole and biotite was performed using a JEOL JXA-8200 microprobe equipped with five spectrometers and TAP, PET, LDE1, PETJ and LIF spectrometer crystals, using 15kV, 15 nA and a focused beam. Sodium and K were measured for 10s on peak and 5 s on each background (10 s / 2x5 s); Si, Al, Ti, Fe, Mn, Mg, Ca and Ba were measured for 20 s / 2x10s, and F and Cl for 30 s / 2x15s. Na, Si, Ti, K and Fe were measured first. Standardization was performed on albite (Na), orthoclase (K), diopside (Si, Ca), spinel (Al), $MnTiO_3$ (Mn, Ti), andradite (Fe), forsterite (Mg), barite (Ba), fluorite (F) and tugtupite (Cl).

In situ Sr-Nd isotopic analysis of apatite
In situ Sr-Nd isotopic analysis of apatite was performed on polished sections of 100-150 μm thickness, using a Neptune Plus MC-ICP-MS coupled to a 193 nm Excimer ArF laser ablation system at State Key Laboratory of Lithospheric Evolution, Institute of Geology and Geophysics, Chinese Academy of Sciences (CAS), Beijing. Detailed instrumental operating conditions can be found in Yang et al. (2008, 2014), and are briefly summarized here. A laser spot of 60-120 μm was employed with an 8 Hz repetition pulse rate and an energy density of 10 J/cm^2, depending on the size and Sr content of apatite grains. The sample chamber was flushed with He gas at a rate of 0.8 to 0.9 Lmin^{-1}. Each measurement is composed of 40 s analysis of the Kr gas blank with the laser switched off, followed by 60 s of analysis with the laser turned on. AP1 apatite (Yang et al. 2008, 2014), was used as external standard. As documented by Yang et al. (2014), Sr isotope analysis can be affected by interferences from Kr, Yb^{2+}, $Er^{2+}$and Rb. The isobaric interference of ^{84}Kr and ^{86}Kr on ^{84}Sr and ^{86}Sr was corrected by the natural Kr isotopic ratios of $^{83}Kr/^{84}Kr = 0.20175$ and $^{83}Kr/\ ^{86}Kr = 0.66474$, respectively. As apatite commonly is REE-rich, high contents of Yb and Er can have an influence on the Sr isotope composition. The presence of $^{167}Er^{2+}$, $^{171}Yb^{2+}$ and $^{173}Yb^{2+}$ at masses 83.5, 85.5 and 86.5 may contribute a certain amount of $^{83}Kr^+$, $^{84}Sr^+$, $^{85}Rb^+$, $^{86}Sr^+$, $^{87}Sr^+$ and $^{88}Sr^+$ (Ramos et al. 2004). The influence of $^{166}Er^{2+}$, $^{168}Er^{2+}$and $^{170}Er^{2+}$ on $^{83}Kr^+$, $^{84}Sr^+$ and $^{85}Rb^+$, respectively, was corrected by monitoring the interference

free $^{167}Er^{2+}$ signal intensity and using the isotopic abundances of Er and Yb. The contributions of $^{170}Yb^{2+}$ to $^{85}Rb^{+}$, $^{172}Yb^{2+}$ to $^{86}Sr^{+}$, $^{174}Yb^{2+}$ to $^{87}Sr^{+}$, and $^{176}Yb^{2+}$ to $^{87}Sr^{+}$ were evaluated and corrected by monitoring the interference-free $^{173}Yb^{2+}$ signal intensity. The isobaric interference of ^{87}Rb on ^{87}Sr was corrected by the natural ratio of $^{85}Rb/^{87}Rb$ = 2.5926. The following formula in an Excel VBA (Visual Basic for Applications) macro program was used to calculate the initial $(^{87}Sr/^{86}Sr)_i$. $(^{87}Sr/^{86}Sr)_i = (^{87}Sr/^{86}Sr) - (^{87}Rb/^{86}Sr)(e^{\lambda t}-1)$, where the decay constant λ equals to 0.0000000000142.

For in situ Nd isotopic analysis, a laser spot of 60-120 μm was employed, using a 6 Hz repetition pulse rate and an energy density of 15 J/cm^2, depending on the size of the apatite grain and the Nd content previously determined during the in situ Sr isotope analysis. Helium was used as carrier gas at a rate of 0.7 to 0.8 L min^{-1}. Each analysis incorporated 60 s of data acquisition from the sample. AP2 apatite (Yang et al. 2008, 2014) was used as external standard. In addition, AP1 apatite (Yang et al. 2008, 2014), was analyzed as an unknown in every analytical session. The $^{147}Sm/^{144}Nd$ and $^{143}Nd/^{144}Nd$ ratios of AP1 apatite were 0.0819 ± 0.0001(2SD, n=3) and 0.511330 ± 0.000043(2SD, n=3), which are consistent with the corresponding reference values ($^{147}Sm/^{144}Nd$= 0.0822 ± 14, $^{143}Nd/^{144}Nd$= 0.511349 ± 38) determined by MC-ICP-MS (Yang et al. 2014). The isobaric interference of ^{144}Sm on the ^{144}Nd signal is corrected by the method described by Yang et al. (2014). Data reduction was again performed on an Excel VBA macro program, using the following formulas: $(^{143}Nd/^{144}Nd)i=(^{143}Nd/^{144}Nd)-(^{147}Sm/^{144}Nd)(e^{\lambda t}-1)$, where the decay constant λ= 0.00000000000654;

$\varepsilon Nd(t)= [(^{143}Nd/^{144}Nd)_i /(^{143}Nd/^{144}Nd)_{CHUR,t}-1]\times 10^4$, where $(^{143}Nd/^{144}Nd)_{CHUR,t} = 0.512638-0.1967(e^{\lambda t}-1)$.

Sr-Nd isotopic analysis of amphibole separates

From two amphibole-rich cumulate samples (K6-55 and K6-69) about 400-500 g of material each were crushed, sieved, and then separated by flotation and electromagnetic separation methods. Optically homogeneous amphibole grains were then handpicked under a binocular microscope. From amphibole megacrysts (samples K6-45, K6-52 and K6-53), crystal fragments larger than or equal to 1 cm were selected and then crushed. About 20-30 g of amphibole separates from each sample were prepared for Sr-Nd isotopic analysis. Sr-Nd isotopic analyses were performed at the Isotope Super-clean Laboratory, Peking University, Beijing. Prior to dissolution, amphibole separates were cleaned in an ultra-sonic bath in dilute HNO_3 and then in Milli-Q 18.2 MΩ water for 10-15 min each. Amphibole chips (<20 mesh) were dissolved using acid (HF + $HClO_4$) in sealed Savillex beakers on a hot plate for eight days. Separation of Rb, Sr and light rare earth elements (LREEs) was achieved using a cation-exchange column. Sm and Nd were further purified using a second cation exchange column, conditioned and eluted with dilute HCl. Sr and Nd isotopic ratios were measured using a Nu Plasma II MC-ICP-MS. The measured $^{87}Sr/^{86}Sr$ and $^{143}Nd/^{144}Nd$ values were normalized to $^{86}Sr/^{88}Sr$=0.1194 and $^{146}Nd/^{144}Nd$=0.7219, respectively. The BCR-2 standard material was repeatedly analyzed during each session, giving average $^{87}Sr/^{86}Sr$ and $^{143}Nd/^{144}Nd$ ratios of 0.512633 ± 0.000011 (±2σ) and 0.715020 ± 0.000009 (±2σ), respectively. The final data reduction was performed on an Excel VBA (Visual Basic for Applications) macro program, where the following formulas are used.

$(^{87}Sr/^{86}Sr)i=(^{87}Sr/^{86}Sr) - (^{87}Rb/^{86}Sr)(e^{\lambda t}-1)$, where the decay constant $\lambda=0.0000000000142$.
$(^{143}Nd/^{144}Nd)i=(^{143}Nd/^{144}Nd)-(^{147}Sm/^{144}Nd)(e^{\lambda t}-1)$, where the decay constant $\lambda=0.00000000000654$;
$\varepsilon Nd(t)= [(^{143}Nd/^{144}Nd)i /(^{143}Nd/^{144}Nd)_{CHUR,t}-1]\times10^4$, where $(^{143}Nd/^{144}Nd)_{CHUR,t} = 0.512638-0.1967(e^{\lambda t}-1)$.
For the data calculation, the concentrations of Rb, Sr, Sm and Nd in each amphibole separate must be known. These values were determined by LA-ICP-MS, using the analytical protocol described in Du et al. (2018).

1.2. Thermobarometry

The following methods were applied to estimate the P-T-fO_2 conditions of magma crystallization: (1) Clinopyroxene–liquid thermobarometry (Neave and Putirka, 2017), (2) Amphibole–liquid thermobarometry (Putirka 2016), and (3) Magnetite–liquid oxybarometry (Arató and Audétat, 2018). The first two methods were based on mineral compositions determined by electron microprobe analysis, whereas the latter method was based on LA-ICP-MS analyses of entire, unexposed inclusions to circumvent re-equilibration and exsolution effects during cooling.

For clinopyroxene-liquid thermobarometry we used the approach described in Neave and Putirka (2017), utilizing the spreadsheet provided with that study. However, whereas Neave and Putirka (2017) tested in their case study all individual whole-rock compositions to identify the best-matching liquid composition (defined by an equilibrium iron–magnesium exchange coefficient ($K_{D(Fe-Mg)}$) of 0.27±0.03), we related all elements numerically to SiO_2 based on fitting equations in Harker diagrams, and then SiO_2 was varied via goal seek until an equilibrium $K_{D(Fe-Mg)}$ value is found. Mineral compositions for which no matching liquid composition could be found using this constraint were discarded. The clinopyroxene-liquid thermobarometer was calibrated to an uncertainty of ±1.4 kbar and ca. ±30 °C (Putirka, 2008; Neave and Putirka, 2017). For the calculations we assumed a melt H_2O content of 5 wt%. Varying this value by ±2 wt% H_2O results in a temperature change of ±25 °C and a pressure change of ±0.3 kbar.

For amphibole–liquid thermobarometry we used the spreadsheet provided by Putirka (2016). As a first step, a pressure- and liquid-independent temperature is calculated, and this temperature is then used in conjunction with potential liquid compositions and an equilibrium $K_{D(Fe-Mg)}$ value of 0.28±0.11 to calculate pressure. Again, whole-rock compositions were numerically related to SiO_2, and SiO_2 was then varied via goal seek until an equilibrium $K_{D(Fe-Mg)}$ value was found. Amphibole compositions for which no equilibrium liquid composition could be found were discarded. This thermobarometer is associated with an uncertainty of ±2-4 kbar and ca. ±30 °C (Putirka, 2016). However, while the calculated temperatures are robust, the calculated pressures depend strongly on melt H_2O content, which was again set to 5 wt%. Changing this value by ±2 wt% H_2O results in a pressure change of ±0.8-1.3 kbar.

Oxygen fugacity was calculated based on the exchange coefficient of iron and titanium between magnetite and silicate melt (FeTiMM; Arató and Audétat, 2017). Magnetite was analyzed by drilling entire, unexposed inclusions out of the clinopyroxene host and reconstituting their original composition by integrating the signal and numerically

subtracting ablated host. The composition of the coexisting silicate melt was constrained by either taking the average SiO_2 content of melt inclusions (sample K6-69) and combining this information with the whole-rock trends, or by taking the average liquid composition derived by clinopyroxene-liquid thermobarometry (samples ZK207-1 and K6-68). The FeTiMM method was calibrated to an uncertainty of ±0.5 log units fO_2 (Arató and Audétat, 2017), but taking into consideration the uncertainty in constraining the composition of the coexisting silicate melt the overall uncertainty in the present study is probably rather ±0.8 log units.

1.3. Isotopic mixing curve

To examine the extent of potential crustal assimilation in the Tongling magmas, a mixing model analogue to that described in Ma et al. (2000) was used. In our model, the average composition of the Jiaochong gabbro porphyry (equivalent to sample K6-68) was selected as mantle-derived endmember (Du et al. 2018), whereas the averages of the Archean Kongling group rocks (Ma et al. 2000) and Proterozoic Dongling group rocks (Xing and Xu, 1994) were selected as crustal endmembers. The choice of the latter reservoirs is based on the reconstructed crustal structure below Tongling (Tang et al., 1998; Du et al., 2014), combined with our estimated magma crystallization pressures (3.8-5.6 kbar; Table 1). According to Tang et al. (1998), the crust below Tongling remained essentially unchanged since the Mesozoic and is structured as follows (from bottom to top): the lowermost layer (18-32 km depth) is made up of Archean Kongling group rocks, which consist of gneiss, tonalites-trondhjemites-granodiorites (TTG) and minor amphibolites; the next layer (12-18 km depth) is represented by Neoarchean to Paleoproterozoic Dongling group rocks, which consist of gneisses and schists; then comes a layer (8-12 km depth) of Meso- to Neoproterozoic volcano-sedimentary rocks (now gneisses); followed by (4-8 km depth) Mesozoic to Paleozoic marine clastic sedimentary rocks; and finally (0-4 km depth) Mesozoic to Cenozoic continental clastic sedimentary rocks and evaporites. Our estimated magma crystallization pressures of 3.8-5.6 kbar translate to a depth interval of ca.14-21 km (Huang et al. 2013), which comprises both Kongling and Dongling group rocks.

The mixing model requires the following input parameters: (1) the concentrations of Rb, Sr, Sm and Nd in each endmember; and (2) the $^{87}Rb/^{86}Sr$, $^{87}Sr/^{86}Sr$, $^{147}Sm/^{144}Nd$, and $^{143}Nd/^{144}Nd$ ratios in each endmember. The Jiaochong gabbro porphyry contains on average 68 ppm Rb, 970 ppm Sr, 10 ppm Sm, 45 ppm Nd, $^{87}Rb/^{86}Sr=0.26$, $^{87}Sr/^{86}Sr=0.71$, $^{147}Sm/^{144}Nd=0.14$, and $^{143}Nd/^{144}Nd=0.51$. The Kongling group rocks contain on average 49 ppm Rb, 560 ppm Sr, 5.4 ppm Sm, 27 ppm Nd, $^{87}Rb/^{86}Sr=0.26$, $^{87}Sr/^{86}Sr=0.71$, $^{147}Sm/^{144}Nd=0.09$, and $^{143}Nd/^{144}Nd=0.51$. The Dongling group rocks contain on average 37 ppm Rb, 400 ppm Sr, 6.3 ppm Sm, 27 ppm Nd, $^{87}Rb/^{86}Sr=0.33$, $^{87}Sr/^{86}Sr=0.72$, $^{147}Sm/^{144}Nd=0.16$, and $^{143}Nd/^{144}Nd=0.51$. The calculations were performed in four steps: (1) estimation of the concentrations of Rb, Sr, Sm and Nd in each mixture; (2) estimation of the corresponding $^{87}Sr/^{86}Sr$ and $^{143}Nd/^{144}Nd$ ratios; (3) estimation of the corresponding $^{147}Sm/^{144}Nd$ and $^{87}Rb/^{86}Sr$ ratios; and (4) estimation of the corresponding $(^{87}Sr/^{86}Sr)_i$ and $\varepsilon Nd(t= 140\ Ma)$.

1.4. Quantitative sulfide fractionation model

Because the whole-rock data follow similar trends as the experimentally derived liquids lines of descent (Figs. 2a, b), the relationship between magma crystallinity and melt SiO_2 content was based on the experimental data of Ulmer et al. (2018), starting with their 1100 °C run of series FCMB(AuPd). At this temperature, the experimental liquid had a SiO_2 content of 49 wt%, similar to the most mafic melt inclusions in cumulate sample K6-69. These melt inclusions coexist with sulfide inclusions and contain 2300±500 ppm sulfur (supplementary Fig. DR8; supplementary Table DR2), hence the sulfur solubility in the silicate melt at this stage (and, correspondingly, the amount of sulfides precipitating at the start of the fractionation model) is relatively well constrained. The decrease in sulfur solubility during magma fractionation was modeled using the models of Jugo et al. (2010) and Fortin et al. (2015) and whole-rock trends that relate SiO_2 to other melt components such as Al_2O_3, FeO_{tot}, MgO and CaO. The MSS/melt partition coefficients were calculated based on the equations given in Li and Audétat (2015).

1.5. Mass balance calculation for the Tongling district

A minimum estimate of the total volume of ore-forming magma in the Tongling district was obtained by taking the exposed surface area of each mineralized intrusion and multiplying it with its mean diameter. The result is a volume of ~50 km^3. In order to provide the combined 3.3 Mt Cu, 160 t Au, 140 t Ag, and 0.03 Mt Mo of the Tongling district, these ~50 km^3 of magma would need to have contained ~40 ppm Cu, ~2 ppb Au, ~2 ppb Ag, and ~0.4 ppm Mo (assuming 50% extraction and precipitation efficiency). The former two values are similar to the modeled metal concentration in the silicate melt after 20 wt% crystallization (supplementary Fig. DR8), whereas the required Ag concentration is about two orders of magnitude lower than the modeled one. The Mo concentration cannot be reliably predicted by the model because Mo is not very chalcophile and its MSS/melt partition coefficient depends strongly on fO_2. However, mafic alkaline magmas typically contain on the order of 1-3 ppm Mo (Audétat, 2010, 2015; Grondahl and Zajacz, 2017; Zhang and Audétat, 2017b), i.e., significantly more than the required concentration of 0.4 ppm. In summary, the calculations demonstrate that after 20 wt% sulfide-saturated crystallization the residual silicate melt still contained enough metal to produce all the mineralization.

1.6. Abundance of mafic microgranular enclaves

Mafic microgranular enclaves (MMEs) have been reported from four intrusions in the Tonging mining district: (1) the Tongguanshan quartz diorite (Wu et al. 2000; Xu et al. 2004; Du et al. 2004; Qin, 2007; Wu et al. 2010; Chen et al. 2016), (2) the Jiguanshi quartz monzodiorite (Qin, 2007), (3) the Fenghuangshan granodiorite (Qin, 2007; Wu et al. 2010), and (4) the Hucun granodiorite (Qin, 2007). However, they are large and abundant only in the Tongguanshan quartz diorite (where they commonly occur as groups with size of 20-50 cm, seldomly up to 140 cm; see Fig. 3-2-6a, b in Qin, 2007 and Fig. 2 in Du et al. 2004), whereas in the other plutons they are much rarer and generally smaller. In the Fenghuangshan granodiorite they reach max. 7 mm in size (Qin, 2007), and in the Hucun granodiorite and Jiguanshi quartz diorite they measure 2-20 cm (Qin, 2007).

Qin (2007) summarized all types of enclaves at Tongling and concluded that Tongguanshan is the only major host of MMEs.

2. Supplementary Figures

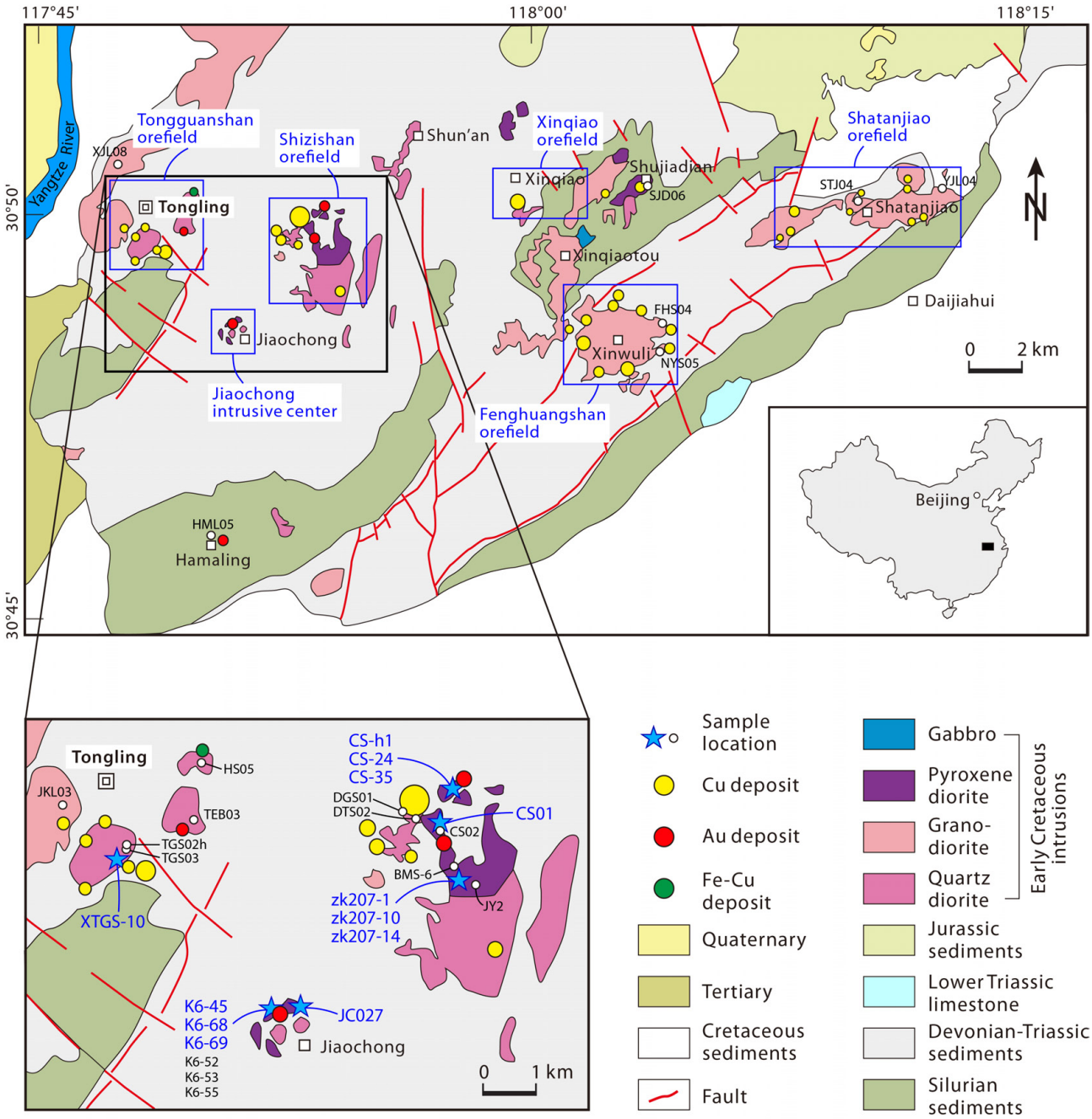

Supplementary Figure DR1 Geological map of the Tongling mining district, modified after Wu et al. (2017). Locations of samples listed in Table 1 are shown by blue stars; locations of the additional samples listed in supplementary Tables DR1, DR3 and supplementary Figure DR8 are shown with white dots.

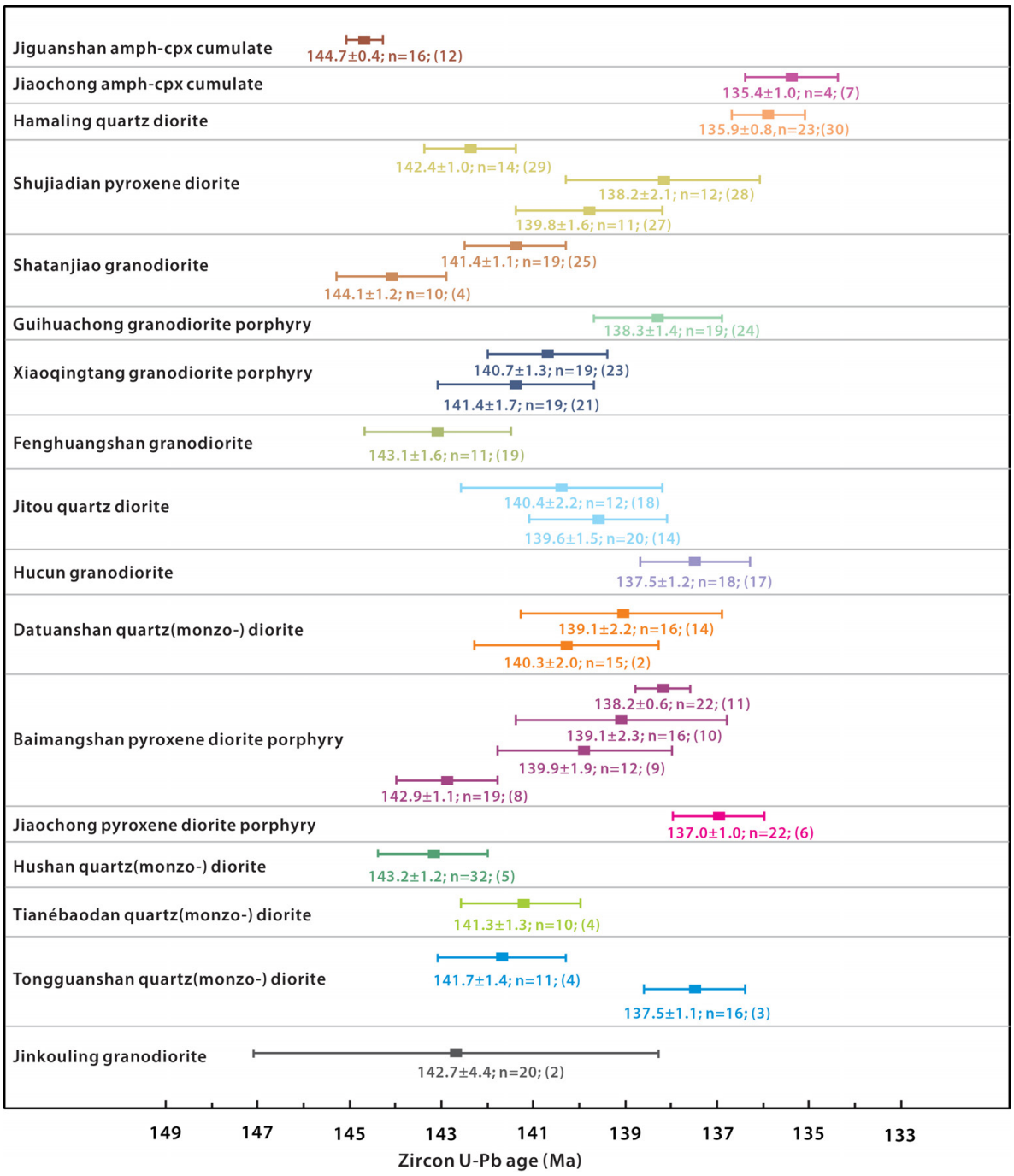

Supplementary Figure DR2 Zircon U-Pb ages of amphibole-clinopyroxene cumulate xenoliths and ore-forming intrusions of Tongling. For each data point the published age, the number of analyzed zircon grains, and the reference number in supplementary Table DR1 is provided.

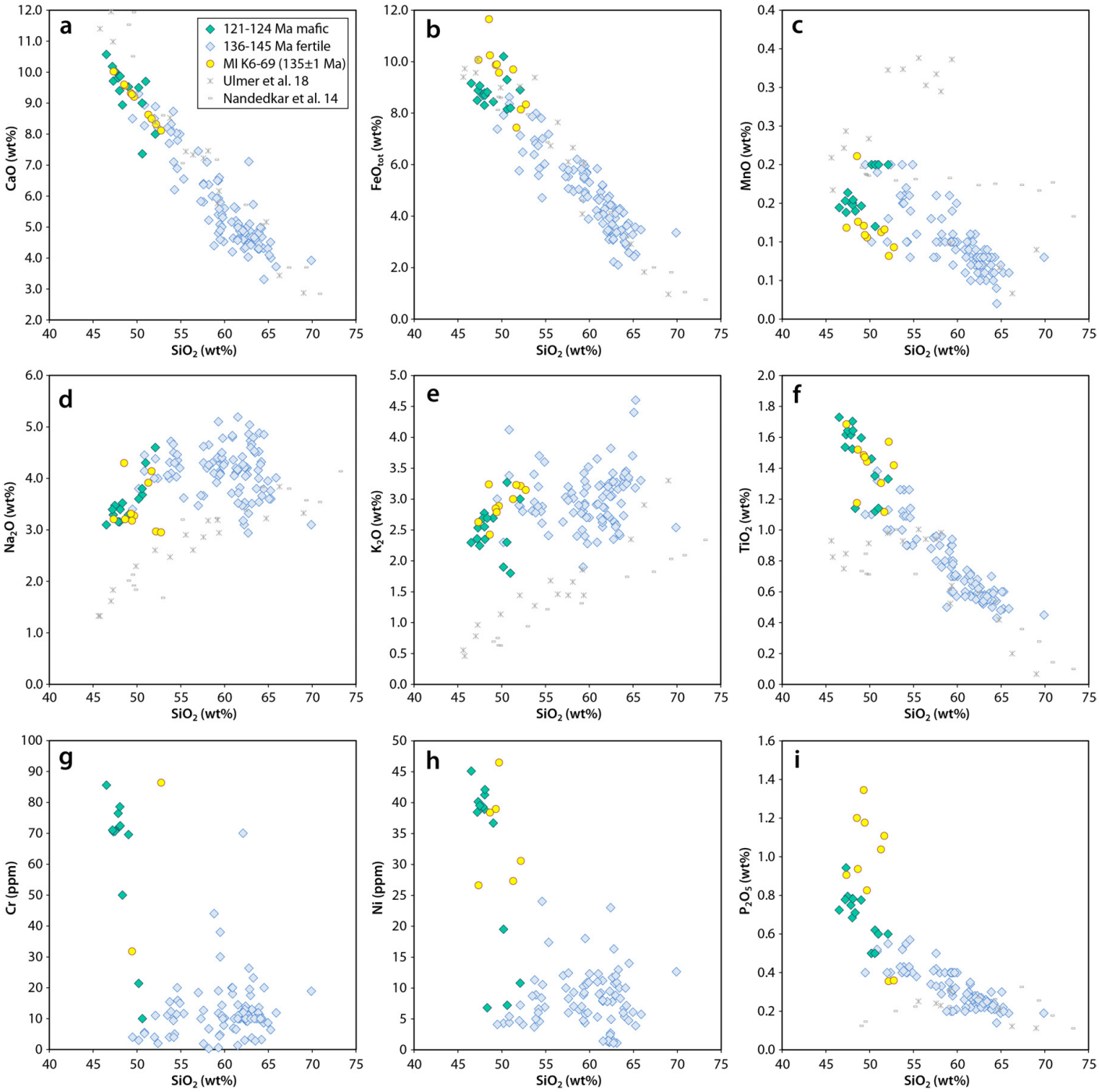

Supplementary Figure DR3 Major- and trace element composition of ore-forming magmas (136-145 Ma), melt inclusions (MI) in a 135±1 Ma cumulate, and 121-124 Ma mafic magmas, compared to experimentally derived fractional crystallization trends of hydrous arc magmas (Nandedkar et al., 2014; Ulmer et al., 2018; series FCMBAuPd). The Tongling whole-rock data are from Wang et al. (2003, 2015, 2016), Huang et al. (2004), Yan et al. (2008), Xie et al. (2012 a, b), Guo et al. (2013), Li et al. (2014), Chen et al. (2016), and Du et al. (2018).

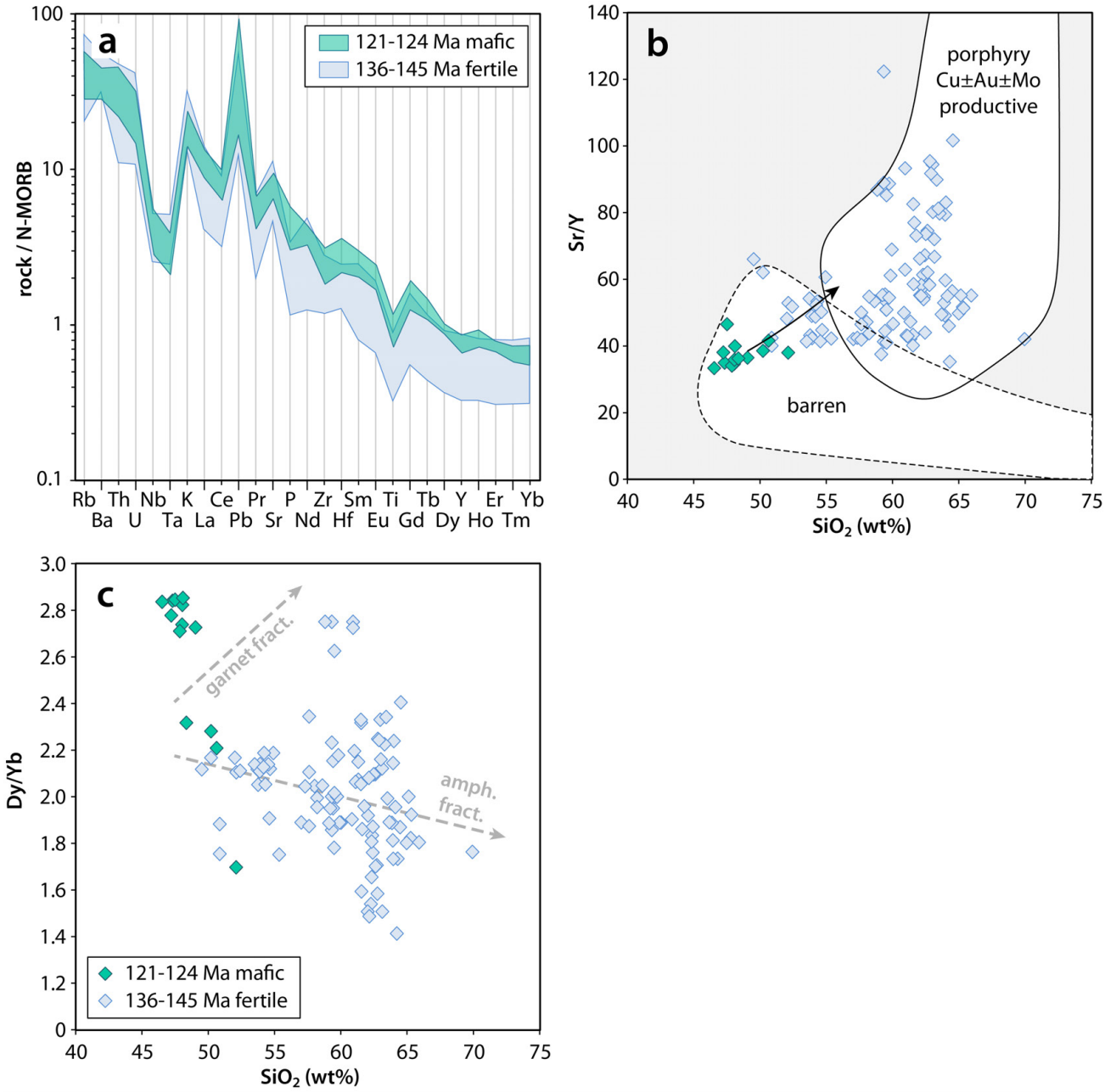

Supplementary Figure DR4 Trace element signature of mafic magmas (121-124 Ma) and ore-forming magmas (136-145 Ma). (**a)** N-MORB normalized spider diagram. The N-MORB reference values are from Gale et al. (2013); (**b)** fields of barren vs. porphyry Cu±Au±Mo productive magmas are from Loucks (2014); the arrow shows the predicted fractionation trend for crystallization of 50 wt% amphibole ($D_{Sr}^{amph/melt} = 0.60$; $D_{Y}^{amph/melt} = 1.2$; $D_{SiO2}^{amph/melt} = 0.80$), 40 wt% clinopyroxene ($D_{Sr}^{cpx/melt} = 0.13$; $D_{Y}^{cpx/melt} = 0.80$; $D_{SiO2}^{cpx/melt} = 1.0$) and 10 wt% magnetite ($D_{Sr}^{mgt/melt} = 0$; $D_{Y}^{mgt/melt} = 0$; $D_{SiO2}^{mgt/melt} = 0$); (**c)** Dy/Yb vs. SiO_2 diagram. Garnet versus amphibole fractionation trends are from Davidson et al. (2007).

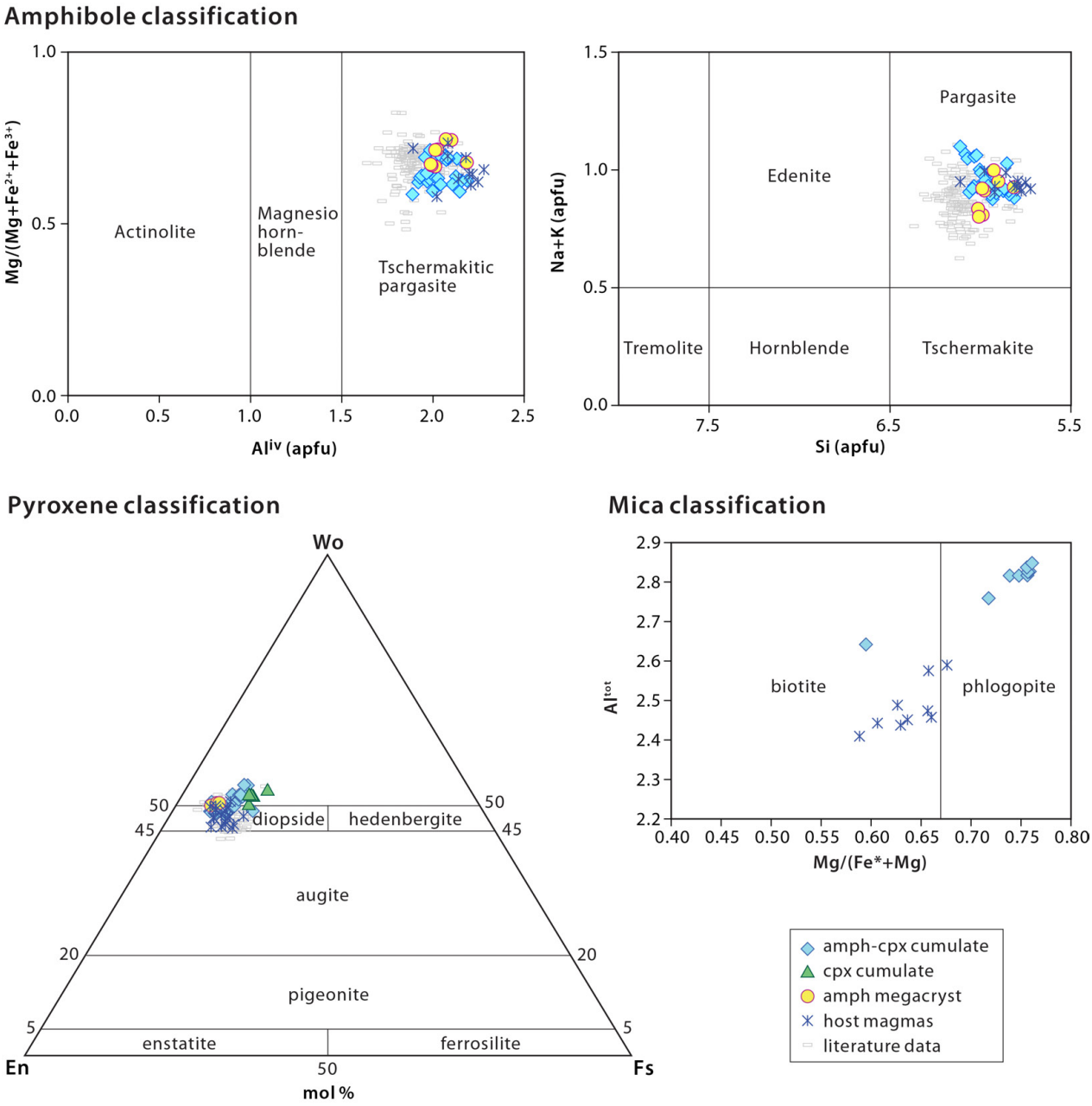

Supplementary Figure DR5 Composition of minerals based on the electron microprobe analyses listed in supplementary Table S4. Amphibole classification is according to Leake et al. (1997; normalization to 23 oxygens); pyroxene classification is according to Sturm (2002; normalization to 6 oxygens); and mica classification is according to Kay et al. (2019; normalization to 22 oxygens; Fe* denotes total Fe expressed as Fe^{2+}).

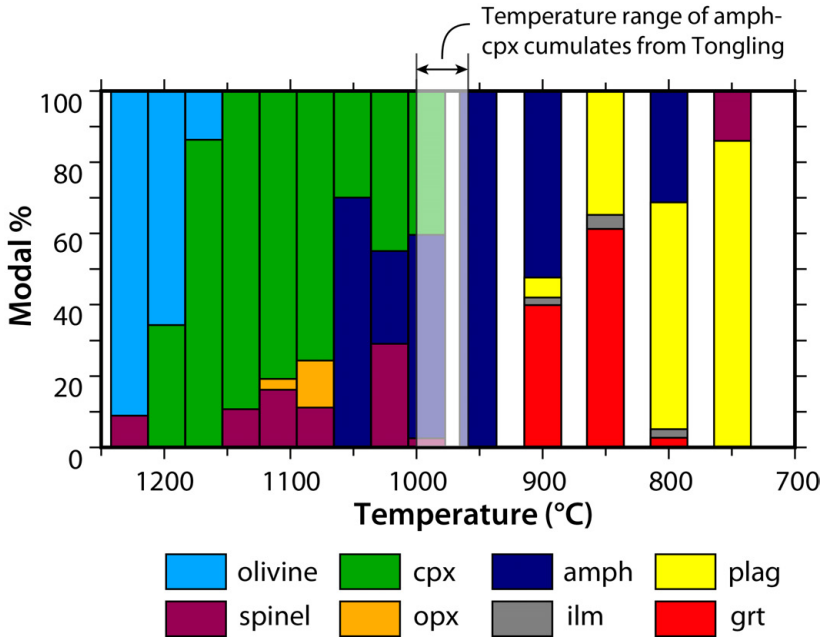

Supplementary Figure DR6 Instantaneous solid composition of the fractional crystallization product (normalized to 100 %) in series MB AuPd of Ulmer et al. (2018), which was conducted at 10 kbar and with 3 wt% H_2O in the starting high-Mg basalt. Cpx – clinopyroxene; opx – orthopyroxene; amph – amphibole; ilm – ilmenite; plag – plagioclase; grt – garnet. The mineral precipitation sequence (cpx –> amph –> plag) and temperature of coexisting amphibole and clinopyroxene agree with the petrologic evidence from the Tongling cumulates.

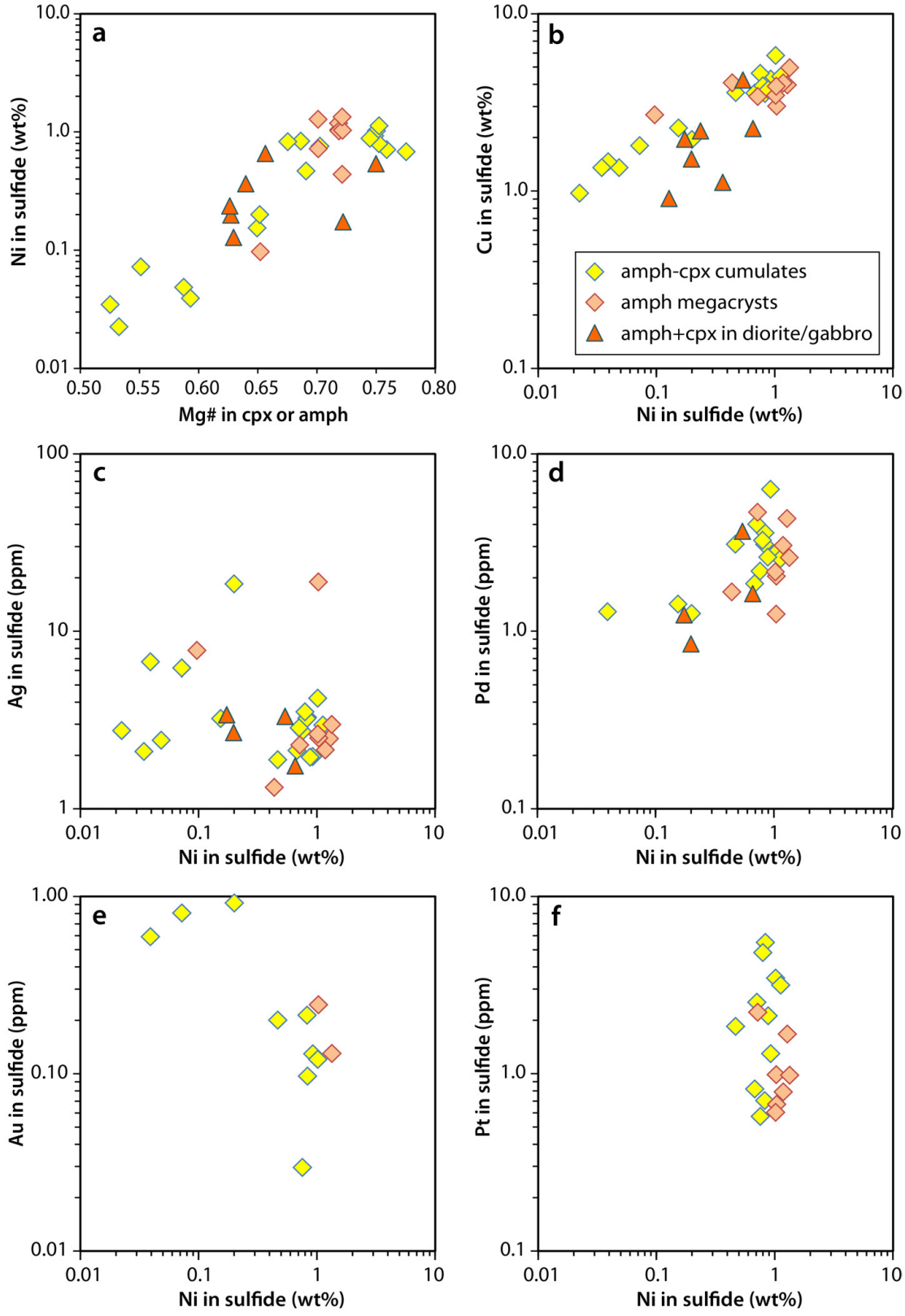

Supplementary Figure DR7 Composition of magmatic sulfides. **(a)** Ni content of magmatic sulfide inclusions (MSS-type) as a function of the Mg# (= molar Mg/(Mg+Fe*)) of the clinopyroxene or amphibole host. **(b-f)** Concentrations of Cu, Ag, Pd, Au and Pt as a function of Ni content.

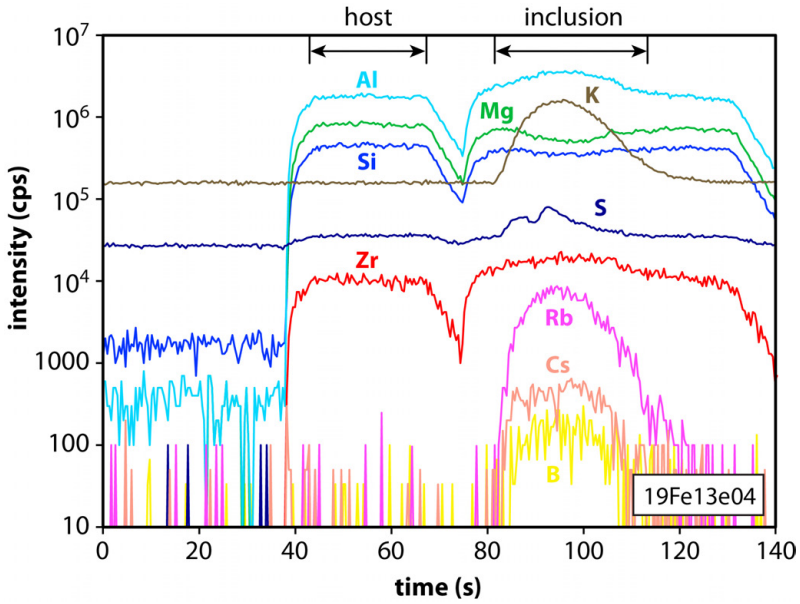

Supplementary Figure DR8 LA-ICP-MS signal of a crystallized silicate melt inclusion hosted in clinopyroxene; cumulate sample K6-69. The melt inclusion measured ca. 37 µm in diameter and contained 47 wt% SiO_2, 17 wt% Al_2O_3, 7.4 wt% MgO, 2.6 wt% K_2O, 2090 ppm S, 270 ppm Zr, 68 ppm Rb, 44 ppm B, and 3 ppm Cs.

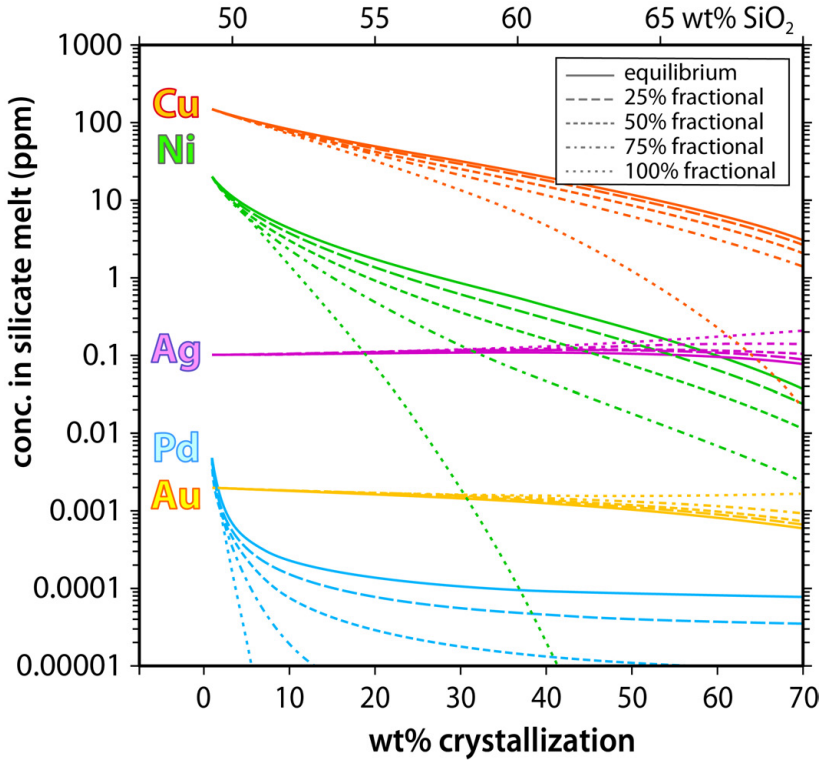

Supplementary Figure DR9 Modeled metal concentrations in the silicate melt as a function of the degree of magma crystallization and the proportion of equilibrium versus fractional sulfide crystallization. The starting concentrations (150 ppm Cu; 20 ppm Ni; 0.1 ppm Ag; 5 ppb Pd; 2 ppb Au) were chosen such to obtain reasonable fits with the natural data points in Figure 3b. They are geologically plausible: 50-300 ppm Cu, 0.05-0.2 ppm Ag, and 1-5 ppb Au are typical for mafic, subduction-related magmas (Grondahl and Zajacz, 2017; Zhang and Audétat, 2017a).

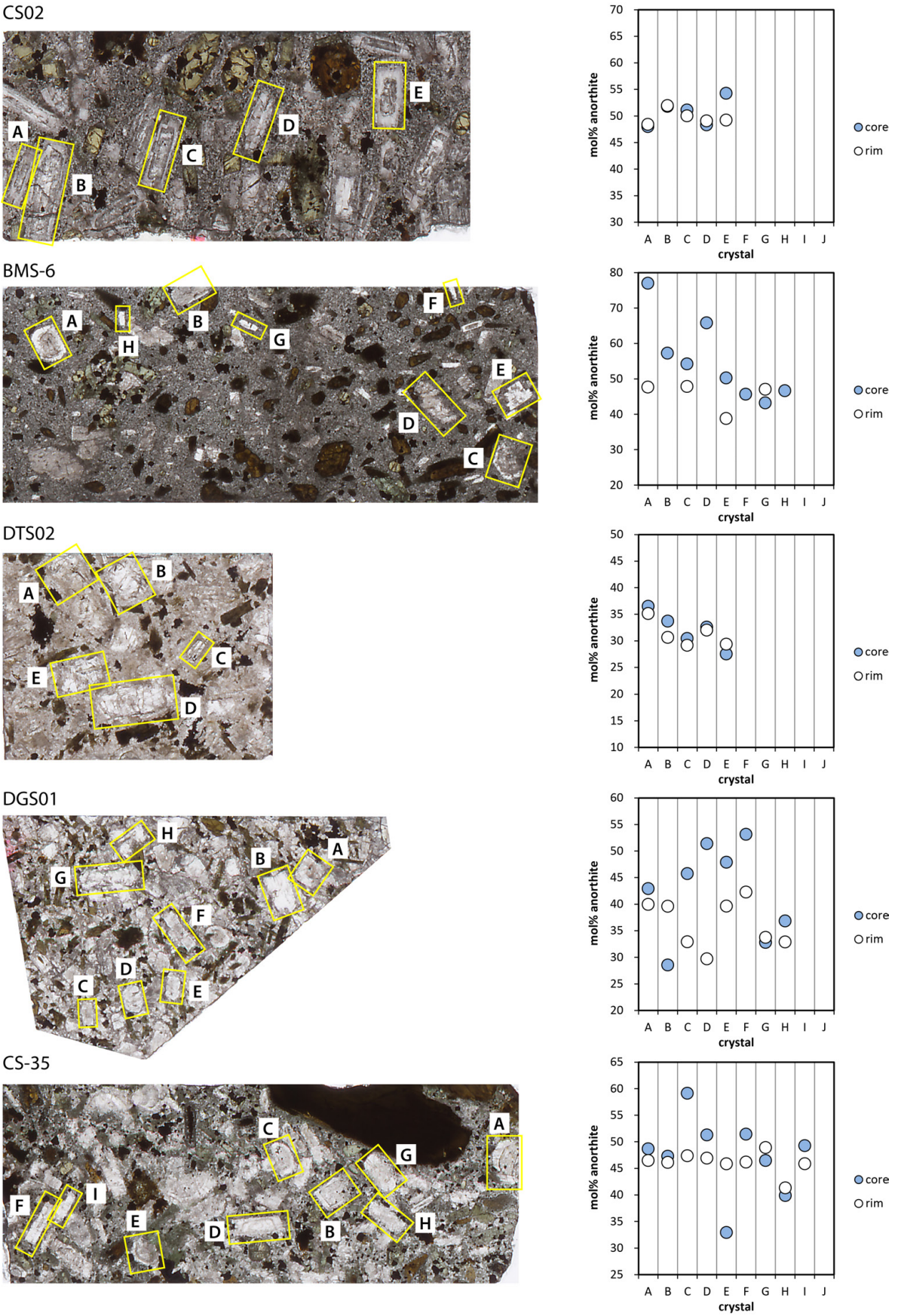

Supplementary Figure DR10 Composition of plagioclase crystals in ore-forming intrusions at Tongling. Although many crystals are optically zoned, the rims show generally equal or lower anorthite contents than cores, hence there is no evidence for late admixture of mafic magma.

JKL03

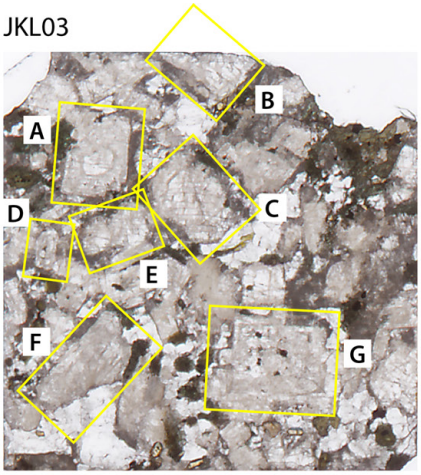

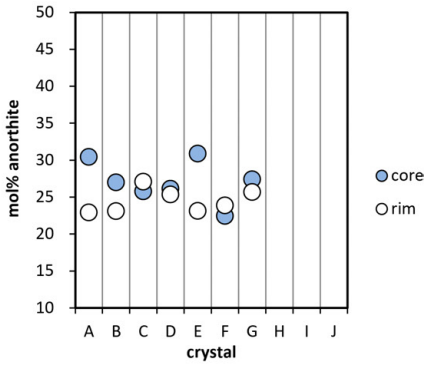

TGS02h

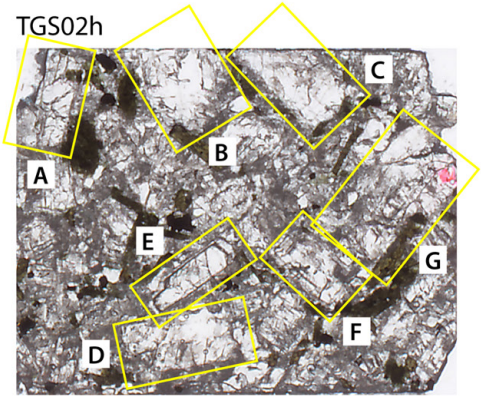

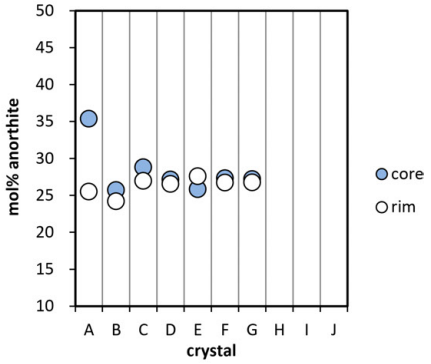

HS05

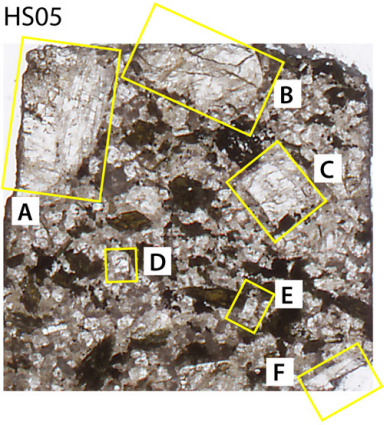

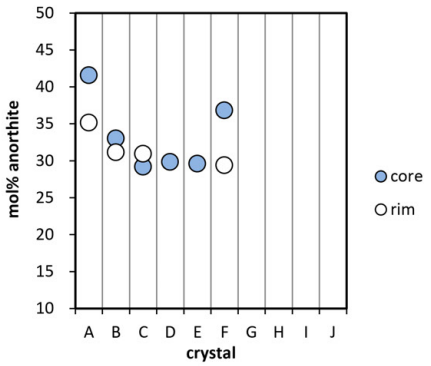

TEB03

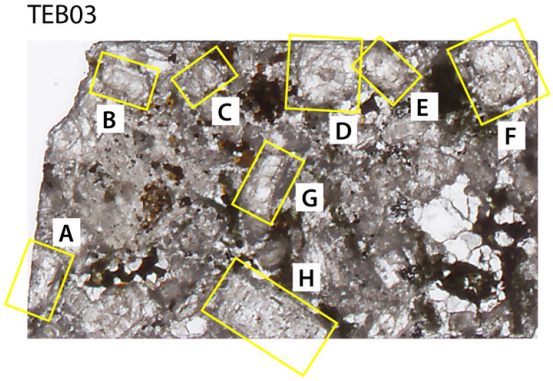

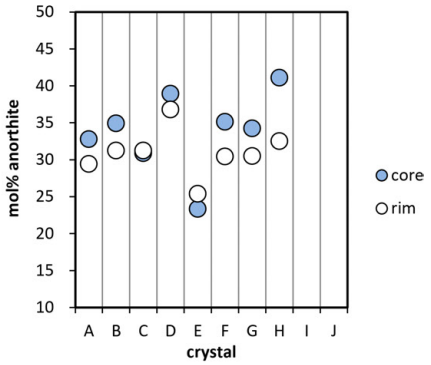

Supplementary Figure DR10 (contd.)

TGS02

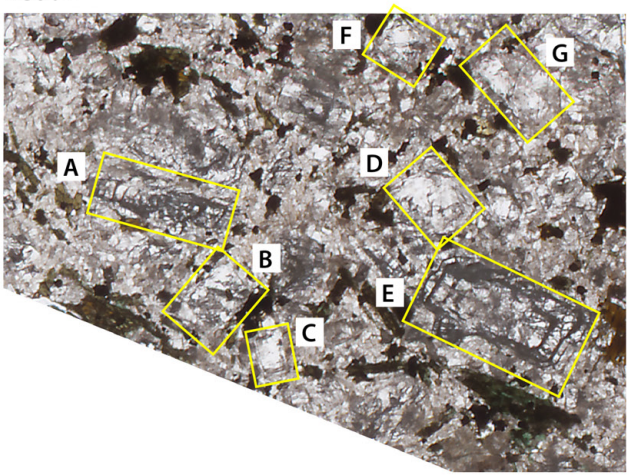

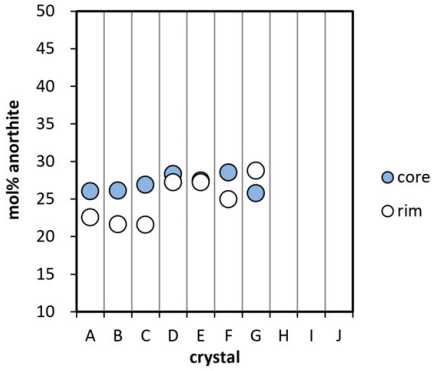

NYS05

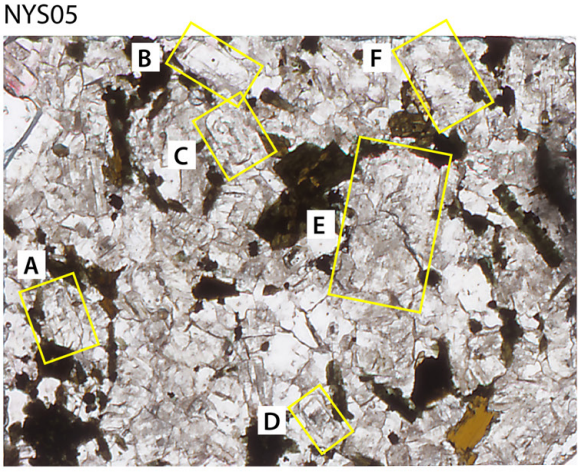

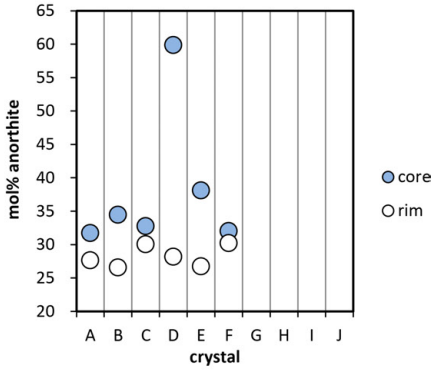

FHS04

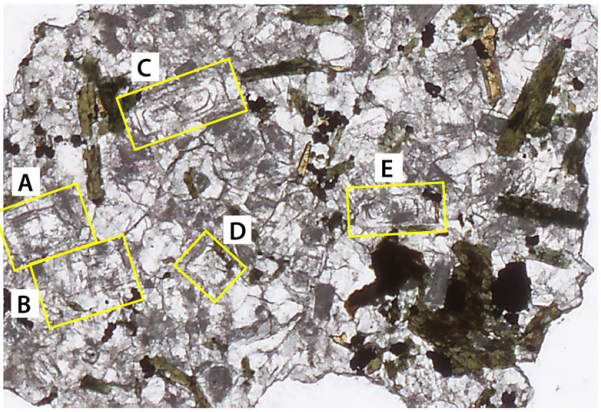

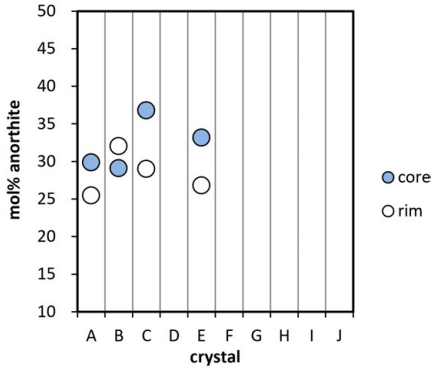

YJL04

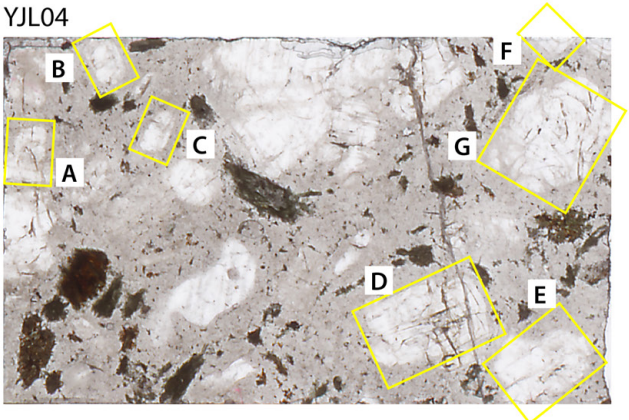

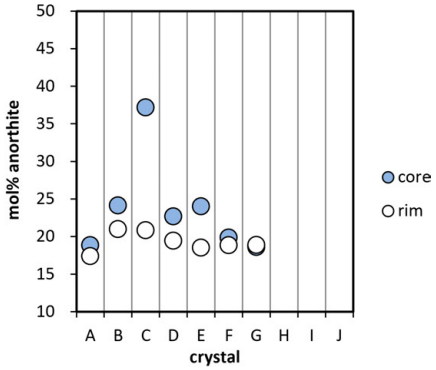

Supplementary Figure DR10 (contd.)

STJ04

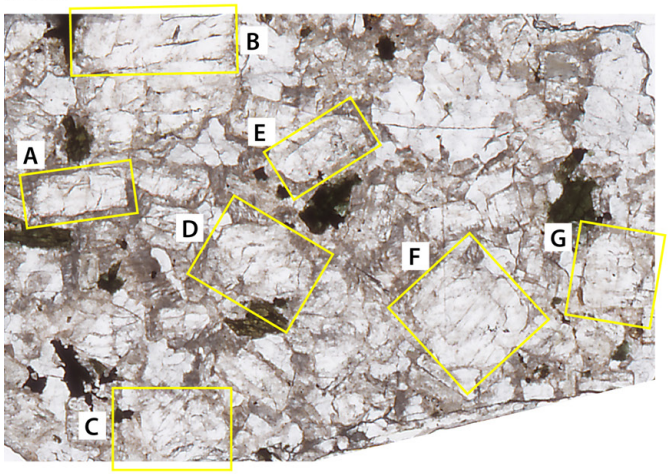

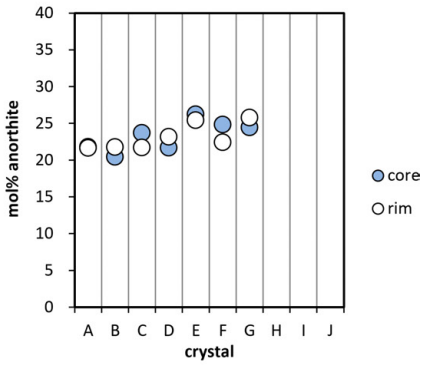

HML05

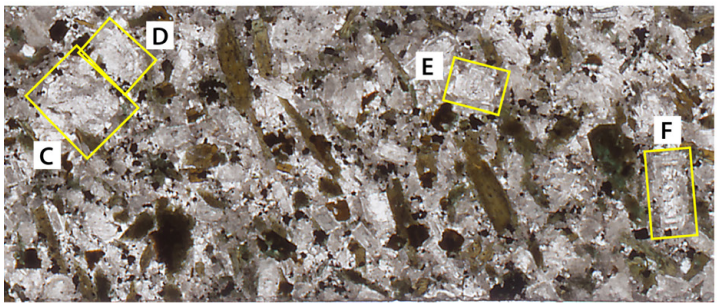

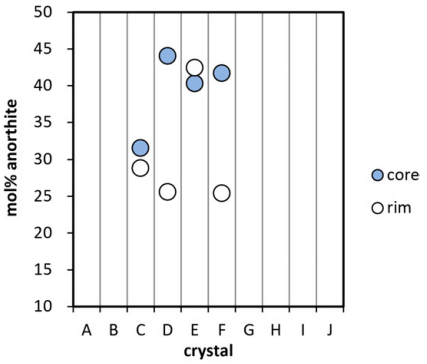

SJD06

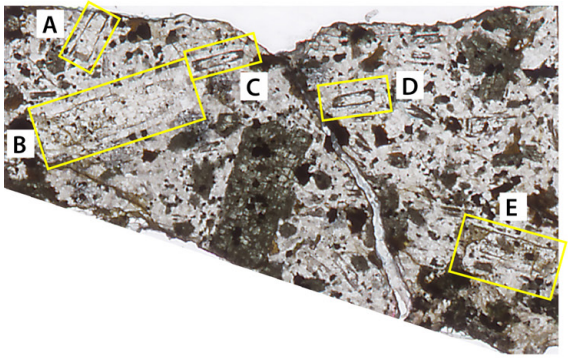

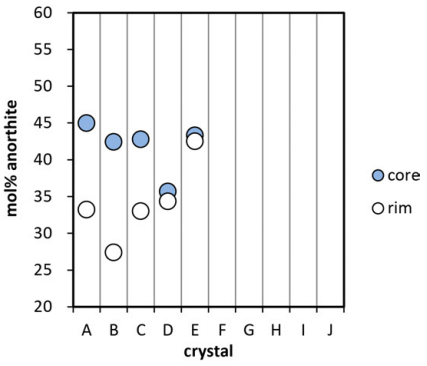

Supplementary Figure DR10 (contd.)

3. Supplementary Tables

Supplementary Table DR1 Overview of ore deposits, related intrusions, and age data of the Tongling mining district

Orefield	Deposit	Deposit age (Ma)	Age Refs	Cu[1] (Mt)	Au[1] (t)	Mo[1] (Mt)	Ore-forming intrusion	Rock type	Rock age (Ma)	Age Refs	Sample (this study)
Tongguan-shan	Jinkouling porphyry-skarn Au(-Cu)	137.0 ± 0.19 (MoS_2 Re-Os)	(1)	0.08	8.6		Jinkouling	Granodiorite	142.7 ± 4.4 (U-Pb zircon)	(2)	JKL03
	Laomiaoji porphyry-skarn Cu +	144.9 ± 0.44 (phlog Ar-Ar)	(1)	0.03			Tongguan-shan	Quartz (monzo-) diorite	137.5 ± 1.1 141.7 ± 1.4 (U-Pb zircon)	(3) (4)	TGS02h
	Xiaotongguanshan porphyry-skarn Cu	135.5 ± 0.45 (phlog Ar-Ar)	(1)	0.06			"	"	"		
	Luocun porphyry-skarn Cu			0.04			"	"	"		
	Bijiashan porphyry-skarn Cu			0.08			"	"	"		
	Huangshilao stratabound Au						"	"	"		
	Tianmashan porphyry-skarn Au				45.8		Tianébao-dan	Quartz (monzo-) diorite	141.3 ± 1.3 (U-Pb zircon)	(4)	TEB03
	Hushan porphyry-skarn Fe-Cu			0.003			Hushan	Quartz (monzo-) diorite/ porphyry	143.2 ± 1.2 (U-Pb zircon)	(5)	HS05
Jiaochong	Jiaochong porphyry-skarn Au				5.9		Jiaochong diorite	Pyroxene diorite porphyry	137.0 ± 1.0 (U-Pb zircon)	(6)	JC027
							N/A	Pyroxene gabbro	120.6 ± 1.2 (U-Pb zircon)	(7)	K6-68
							N/A	Amph-cpx cumulate	135.4 ± 1.0 (U-Pb zircon)	(7)	K6-69 K6-45
Shizishan	Chaoshan porphyry-skarn Au				8.57		Baimang-shan	Pyroxene diorite porphyry	142.9 ± 1.1 139.9 ± 1.9 139.1 ± 2.3 138.2 ± 0.6 (U-Pb zircon)	(8) (9) (10) (11)	CS02 BMS-6
								Amph-cpx cumulate			CS01
	Jiguanshan porphyry-skarn Fe-Au				0.2		"	"	"		
							N/A	Amph-cpx cumulate	144.7 ± 0.4 (U-Pb zircon)	(12)	ZK207-1 ZK207-10 ZK207-14
	Dongguashan porphyry-skarn Cu	137.4 (FeS_2 Re-Os)	(1)	0.94	22		Datuan-shan	Quartz (monzo-) diorite	140.3 ± 2.0 139.1 ± 2.2 (U-Pb zircon)	(2) (14)	DGS01 DGS07
	Huashupo porphyry-skarn Cu			0.1			"	"	"		
	Datuanshan stratabound Cu-(Mo)	139.3 ± 2.6 139.2 ± 0.9 (MoS_2 Re-Os)	(15) (16)	0.27		0.02	"	"	"		DTS02
	Hucunnan porphyry Cu-Mo	139.5 ± 1.1 (MoS_2 Re-Os)	(17)				Hucun	Granodiorite	137.5 ± 1.2 (U-Pb zircon)	(17)	HC-8
	Baocun skarn Au				4.24		Baocun	Diorite porphyry	137 (WR Ar-Ar)	(13)	
	Caoshan porphyry-skarn Au				5.74		Caoshan	Pyroxene diorite porphyry	137 (WR Ar-Ar)	(13)	CS-35
							N/A	Amph-cpx cumulate	140 (WR Rb-Sr)	(13)	CS-35 CS-h1 CS-24
	Shizishan East breccia Cu			0.13			Shizishan	Quartz monzo-diorite			
	Hucun porphyry-skarn Cu			0.08			Hucun	Granodiorite			
	Jiguanshi skarn Ag-Au				0.5		Jiguanshi	Quartz monzo-diorite			

Supplementary Table DR1 (contd.)

Orefield	Deposit	Deposit age (Ma)	Age Refs	Cu[1] (Mt)	Au[1] (t)	Mo[1] (Mt)	Ore-forming intrusion	Rock type	Rock age (Ma)	Age Refs	Sample (this study)
Xinqiao	Xinqiao porphyry-skarn Cu-S-Fe-Au	138.0 ± 2.3 (Fi Rb-Sr) 138 ± 26 FeS_2 (Re-Os)	(14) (18)	0.5	11.2		Jitou	Quartz diorite	139.6 ± 1.5 140.4 ± 2.2 (U-Pb zircon)	(14) (18)	
Fenghuang-shan	Fenghuangshan porphyry-skarn Cu	141.7 ± 0.8 (MoS_2 Re-Os)	(19)	0.42			Fenghuang-shan	Granodiorite	143.1 ± 1.6 (U-Pb zircon)	(19)	
	Tieshantou porphyry-skarn Cu			0.06			"	"			
	Lanhuachong porphyry-skarn Cu			0.02			"	"			
	Xianrenchong porphyry-skarn Cu	140.9 ± 2.2 (MoS_2 Re-Os)	(20)	0.08			"	"			FHS04
	Baoshantao porphyry-skarn Cu			0.09			"	"			
	Zhujiashan porphyry-skarn Cu			0.01			"	"			
	Nanyangshan porphyry-skarn Cu	140.5 ± 1.6 (MoS_2 Re-Os)	(15)	0.01			"	"			NYS05
Shatanjiao	Yaojialing porphyry-skarn Zn-Au	141.2 ± 2.1 141.6 ± 2.7 141.6 ± 0.9 (MoS_2 Re-Os)	(21) (22)		32.2		Xiaoqing-tang	Granodiorite porphyry	141.4 ±1.7 140.7 ±1.3 (U-Pb zircon)	(21) (23)	YJL04 YJL05
	Guihuachong porphyry-skarn Cu						Guihua-chong	Granodiorite porphyry	138.3 ±1.4 (U-Pb zircon)	(24)	GHC-2
	Shatanjiao porphyry-skarn Cu	140.3 ± 1.8 (MoS_2 Re-Os)	(15)				Shatanjiao	Granodiorite	144.1 ± 1.2 141.4 ± 1.1 (U-Pb zircon)	(4) (25)	STJ04
Shujiadian	Shujiadian porphyry Cu	140.6 ± 2.0 (MoS_2 Re-Os)	(26)	0.37			Shujiadian	Pyroxene diorite	139.8 ± 1.6 138.2 ± 2.1 142.4 ± 1.0 (U-Pb zircon)	(27) (28) (29)	SJD05 SJD06
Meijiashan	Meijiashan Au				0.13						
Hamaling	Hamaling porphyry-skarn Au	141.1 ± 1.7 (MoS_2 Re-Os)	(30)		N/A		Hamaling	Quartz diorite	135.9 ± 0.8 (U-Pb zircon)	(30)	HML05

Abbreviations: phlog – phlogopite; Fi – Fluid inclusions; WR – whole-rock; Amph – amphibole; cpx – clinopyroxene
[1] Source: Chinese National Geological Archives (NGA) http://www.ngac.cn

References

(1) Meng, Y., Yang, Z., Zeng, P., Xu, W. & Wang, X. Tentative temporal constraints of ore-forming fluid systems in Tongling metallogenic province. *Miner. Deposita* **23**, 271-280 (2004). (in Chinese with English abstract)

(2) Xie, J., Wang, Y., Li, Q., Yan, J. & Sun, W. Petrogenesis and metallogenic implications of late Mesozoic intrusive rocks in the Tongling region, Eastern China: a case study and perspective review. *Int. Geol. Rev.* **60**, 1361-1380 (2018)

(3) Xu, X. et al. U-Pb dating of zircons from quartz diorite and its enclaves at Tongguanshan in Anhui and its petrogenetic implication. *Chinese Sci. Bull.* **49**, 2073-2082 (2004)

(4) Wu, C., Dong, S., Wu, D., Zhang, X. & Ernst, W. G. Late Mesozoic high-k calc-alkaline magmatism in Southeast China: the Tongling example. *Int. Geol. Rev.* **60**, 1326-1360 (2018)

(5) Lei, M. et al. Mineral composition and zircon U-Pb dating of Hushan intrusion in Tongling area, Anhui Province. *Geol. in China* **42**, 1274-1292 (2015). (in Chinese with English abstract)

(6) Wu, C., Dong, S. & Guo, X. *Intermediate-acid Intrusive Rocks from Tongling, China* (Geological Publishing House, Beijing, 2013). (in Chinese with English abstract)

(7) Du, J., Du, Y. & Cao, Y. Important role of hornblende fractionation in generating the adakitic magmas in Tongling, Eastern china: evidence from amphibole megacryst and cumulate xenoliths and host gabbros. *Int. Geol. Rev.* **60**, 1381-1403 (2018)

(8) Wang, Y., Liu, D., Zeng, P., Yang, Z. & Tian, S. SHRIMP U-Pb Geochronology of pyroxene diorite in the Chaoshan gold deposit and its geological significance. *Acta. Geos. Sin.* **25**, 423-427 (2004). (in Chinese with English abstract)

(9) Wu, C. et al. Zircon SHRIMP U-Pb dating of intermediate-acid intrusive rocks from Shizishan, Tongling and the deep processes of magmatism. *Acta. Petrol. Sin.* **24**, 1801-1812 (2008). (in Chinese with English abstract)

(10) Xu, X., Lu, S., Xie, Q., Bai, L. & Chu, G. SHRIMP Zircon U-Pb dating for the magmatic rocks in Shizishan orefield of Tongling, Anhui province, and its geological implications. *Acta. Geol. Sin.* **82**, 500-509 (2008). (in Chinese with English abstract)

(11) Guo, H., Lu, J., Jiang, S., Zhang, R. & Zhao, Z. Chronology, Hf isotopes, geochemistry, and petrogenesis of the magmatic rocks in the Shizishan ore field of Tongling, Anhui province. *Sci. China Earth Sci.* **56**, 993-1013 (2013)

(12) Hu, L., Li, Y., Song, Y. & Wang, A. Zircon U-Pb dating and mineral Chemistry of the amphibole cumulates in Tongling, Anhui Province, and its implications for deep magmatism. *Acta. Geol. Sin.* **92**, 704-721 (2018). (in Chinese with English abstract)

(13) Tang, Y. et al. *Geology of Copper-Gold Polymetallic Deposits in the Along-Changjiang Area of Anhui Province* (Geological Publishing House, Beijing, 1998). (in Chinese with English abstract)

(14) Wang, S. et al. Petrogenesis of Dongguashan skarn-porphyry Cu–Au deposit related intrusion in the Tongling district, eastern China: Geochronological, mineralogical, geochemical and Hf isotopic evidence. *Ore. Geol. Rev.* **64**, 53–70 (2015)

(15) Mao, J. et al. Molybdenite Re–Os and albite $^{40}Ar/^{39}Ar$ dating of Cu–Au–Mo and magnetite porphyry systems in the Yangtze River Valley and metallogenic implications. *Ore. Geol. Rev.***29**, 307–324(2006)

(16) Cao, Y., Gao, F., Du, Y., Du, Y. & Pang, Z. Genesis of the Datuanshan stratabound skarn Cu (–Mo) deposit, middle–lower Yangtze Valley, Eastern China: constraints from geology, Re–Os geochronology, mineralogy, and sulfur isotopes. *Miner. Deposita* **52**, 1-20

(17) Yang, H. et al. U-Pb and Re-Os geochronology of the Hucunnan Copper-Molybdenum deposit in Anhui province, Southeast China, and its geological implications. *Resour. Geol.* **66**, 303-312 (2016)

(18) Zhang, Y., Shao, Y., Li, H. & Liu, Z. Genesis of the Xinqiao Cu–S–Fe–Au deposit in the Middle-lower Yangtze River Valley metallogenic belt, Eastern China: constraints from U–Pb–Hf, Rb–Sr, S, and Pb isotopes. *Ore. Geol. Rev.***86**, 100-116 (2017)

(19) Li, S., Yang, X., Huang, Y. & Sun, W. Petrogenesis and mineralization of the Fenghuangshan skarn Cu–Au deposit, Tongling ore cluster field, Lower Yangtze metallogenic Belt. *Ore. Geol. Rev.***58**, 148–162 (2014)

(20) Wang, C. et al. Ore-forming ages and sources of metallogenic materials of Fenghuangshan orefield in Tongling. *Miner. Deposita* **37**, 1195-1216 (2018). (in Chinese with English abstract)

(21) Zhong, G. et al. LA-ICP-MS zircon age and molydenite Re-Os dating of Yaojialing large zinc-gold polymetallic deposit, Tongling, Anhui Province, China. *Acta. Petrol. Sin.***30**, 1075-1086 (2014). (in Chinese with English abstract)

(22) Yin, Y. et al. The Re-Os age of molydenite and ore-forming material source from the Yaojialing Zn-Au polymetallic deposit, Tongling. *Geol. Rev.* **62**, 248-256 (2016). (in Chinese with English abstract)

(23) Liu, S., Du, Y., Fu, S., Zhong, H. & Cao, Y. U-Pb age and Hf isotopic characteristics of zircons from granodiorite porphyry in the Yaojialing Zn-Au-Polymetallic mine, Anhui province and their geological significance. *J. China. Univ. Geosci. Earth. Sci.***38**, 91-102 (2014). (in Chinese with English abstract)

(24) Yue, Z. et al. Geochemical features and U-Pb age of the Guihuachong granodiorite porphyry in Tongling and their geological implications. *J. Mineral. Petrol.***35**, 82-90 (2015). (in Chinese with English abstract)

(25) Wu, X., Yan, J., Tang, Y., Chu, X. & Peng, G. Geochronology and geochemistry of Shatanjiao granodiorite from Tongling, Anhui province. *J. Mineral. Petrol.***31**, 75-82 (2011). (in Chinese with English abstract)

(26) Wang, S. et al. Re-Os and $^{40}Ar/^{39}Ar$ dating of the Shujiadian copper deposit in Tongling, China: Implications for regional metallogenesis. *Acta. Petrol. Sin.***28**, 3170-3180 (2012).(in Chinese with English abstract)

(27) Wu, C. et al. Petrogenesis of the intermediate-acid intrusive rocks and zircon SHRIMP dating in Tongling, Anhui, China. *Acta. Petrol. Sin.***26**, 2630-2652 (2010). (in Chinese with English abstract)

(28) Wang, S., Zhou, T., Yuan, F., Fan, Y. & Lü, Y. Geochronology and Geochemical characteristics of the Shujiadian intrusion in Tongling, China. *Acta. Geol. Sin.* **85**, 849-861 (2011). (in Chinese with English abstract)

(29) Wang, S. et al. Geochemical characteristics of the Shujiadian Cu deposit related intrusion in Tongling: Petrogenesis and implications for the formation of porphyry Cu systems in the Middle-Lower Yangtze River Valley metallogenic belt, Eastern China. *Lithos* **252-253**, 185-199 (2016)

(30) Hu, Q. Origin of Hamaling copper-gold deposit in Tongling region and its significance for deep prospecting. Master thesis. China University of Geosciences in Beijing (2018). (in Chinese with English abstract)

Supplementary Table DR2 LA-ICP-MS analyses of clinopyroxene-hosted melt inclusions in sample K6-69

Inclusion	#1	#2	#3	#4	#5	#6	#7	#8	#9	#10
Size (µm)	35	37	45	29	28	26	22	40	40	50
SiO_2 (wt%)	49.7	47.4	49.3	49.4	52.2	52.8	48.7	48.5	51.3	51.7
TiO_2 (wt%)	1.4	1.7	1.5	1.5	1.6	1.4	1.5	1.2	1.3	1.1
Al_2O_3 (wt%)	16.9	16.6	15.9	15.5	17.4	16.2	16.8	14.3	16.3	16.6
FeO_{tot} (wt%)	9.6	10.1	9.9	9.9	8.1	8.3	10.2	11.6	9.7	7.4
MgO (wt%)	6.1	7.4	6.5	7.2	5.7	6.6	6.5	5.8	4.7	6.1
MnO (wt%)	0.1	0.1	0.1	0.1	0.1	0.1	0.1	0.2	0.1	0.1
CaO (wt%)	9.2	10.0	9.3	9.3	8.3	8.1	9.6	9.6	8.6	8.5
Na_2O (wt%)	3.3	3.2	3.3	3.2	3.0	3.0	3.2	4.3	3.9	4.1
K_2O (wt%)	2.9	2.6	2.8	2.8	3.2	3.1	2.4	3.2	3.0	3.2
P_2O_5 (wt%)	0.8	0.9	1.3	1.2	0.4	0.4	0.9	1.2	1.0	1.1
Total (wt%)	100.0	100.0	100.0	100.0	100.0	100.0	100.0	100.0	100.0	100.0
B (ppm)	44	44	46	38	34	42	43	54	49	38
S (ppm)	1800	2100	2600	2800	n.a.	n.a.	n.a.	n.a.	n.a.	n.a.
Cl (ppm)	1100	1100	1200	1500	n.a.	n.a.	n.a.	n.a.	n.a.	n.a.
Cu (ppm)	n.a.	n.a.	n.a.	n.a.	57	66	190	140	110	4
Zn (ppm)	n.a.	n.a.	n.a.	n.a.	80	74	58	103	75	86
Rb (ppm)	81	68	66	67	88	96	68	73	74	76
Sr (ppm)	n.a.	n.a.	n.a.	n.a.	730	770	920	1300	1200	1200
Y (ppm)	n.a.	n.a.	n.a.	n.a.	22	23	49	66	40	26
Zr (ppm)	300	270	290	290	210	260	470	420	300	250
Nb (ppm)	n.a.	n.a.	n.a.	n.a.	14	15	15	19	16	21
Cs (ppm)	2.6	2.7	2.2	2.0	3.4	3.6	2.8	3.4	3.6	2.9
Ba (ppm)	620	530	610	560	490	510	500	620	560	600
La (ppm)	n.a.	n.a.	n.a.	n.a.	58	67	77	140	100	85
Ce (ppm)	n.a.	n.a.	n.a.	n.a.	130	130	170	310	210	170
Ta (ppm)	n.a.	n.a.	n.a.	n.a.	1.2	0.9	0.7	1.0	0.9	1.0
Th (ppm)	n.a.	n.a.	n.a.	n.a.	14	15	11	41	21	13
U (ppm)	n.a.	n.a.	n.a.	n.a.	3.4	3.7	3.8	n.a.	5.5	3.7

Supplementary Table DR3 Isotopic data

Sample type	Analysis type	Sample name	Location	Orefield	$^{7}Sr/^{86}Sr)i$	εNd(t)	Reference
Early Cretaceous cumulates and amphibole megacrysts							
Amph-cpx cumulate	in-situ apa (n=11)	k6-69	Jiaochong	Jiaochong	0.7068	-2.1	(1)
Amph-cpx cumulate	amph separates	K6-69	Jiaochong	Jiaochong	0.7069	-2.1	(1)
Amph-cpx cumulate	amph separates	K6-55	Jiaochong	Jiaochong	0.7067	-3.8	(1)
Amph megacryst	amph separates	K6-45	Jiaochong	Jiaochong	0.7066	-3.5	(1)
Amph megacryst	amph separates	K6-52	Jiaochong	Jiaochong	0.7067	-3.6	(1)
Amph megacryst	amph separates	K6-53	Jiaochong	Jiaochong	0.7069	-3.9	(1)
Cpx cumulate	whole-rock	AC20	Xiaotongguanshan	Tongguanshan	0.7073	-9.7	(2)
Amph-cpx cumulate	in situ apa (n=5)	JY2	Jiguanshan	Shizishan	0.7066	-9.3	(1)
Amph-apa cumulate	in situ apa (n=2)	XJL08-2	Xiejialong		0.7077	-10.5	(1)
Early Cretaceous intrusions							
Gabbro porphyry	whole-rock (n=9)	K6-68	Jiaochong	Jiaochong	0.70694	-3.7	(3)
quartz monzodiorite	whole-rock	TL-7	Tongguanshan	Tongguanshan	0.70728	-13.1	(4)
quartz monzodiorite	whole-rock	TL-13	Tongguanshan	Tongguanshan	0.70756	-12.7	(4)
quartz monzodiorite	whole-rock	TL-14	Tongguanshan	Tongguanshan	0.70736	-13.2	(4)
quartz monzodiorite	whole-rock	TL-15	Tongguanshan	Tongguanshan	0.70736	-13.1	(4)
quartz monzodiorite	whole-rock	TL-17	Tongguanshan	Tongguanshan	0.70740	-12.5	(4)
quartz monzodiorite	whole-rock	TL-20	Tongguanshan	Tongguanshan	0.70742	-13.2	(4)
pyroxene diorite	whole-rock	TL-25	Baimangshan	Shizishan	0.70707	-9.6	(4)
pyroxene diorite	whole-rock	TL-27	Baimangshan	Shizishan	0.70696	-9.5	(4)
pyroxene diorite	whole-rock	TL-32	Baimangshan	Shizishan	0.70676	-9.6	(4)
pyroxene diorite	whole-rock	TL-35	Jiguanshan	Shizishan	0.70724	-12.1	(4)
pyroxene diorite	whole-rock	TL-36	Jiguanshan	Shizishan	0.70727	-12.0	(4)
pyroxene diorite	whole-rock	01TL101	not specified	Tongguanshan	0.70641	-6.6	(5)
pyroxene diorite	whole-rock	01TL102	not specified	Tongguanshan	0.70630	-5.7	(5)
pyroxene diorite	whole-rock	01TL103	not specified	Tongguanshan	0.70564	-5.7	(5)
diorite	whole-rock	01TL072	not specified	Tongguanshan	0.70644	-4.8	(5)
diorite	whole-rock	01TL073	not specified	Tongguanshan	0.70644	-5.7	(5)
diorite	whole-rock	01TL075	not specified	Tongguanshan	0.70625	-4.7	(5)
diorite	whole-rock	01TL078	not specified	Tongguanshan	0.70711	-6.2	(5)
diorite	whole-rock	01TL080	not specified	Tongguanshan	0.70704	-5.8	(5)
pyroxene diorite	whole-rock	TLMS01	Shujiadian	Shujiadian	0.70695	-11.2	(6)
quartz diorite	whole-rock	TLXDGS01	Dongguanshan	Shizishan	0.70710	-12.7	(6)
pyroxene diorite	whole-rock	TLBMS01	Baimangshan	Shizishan	0.70709	-11.8	(6)

Supplementary Table DR3 (contd.)

Sample type	Analysis type	Sample name	Location	Orefield	$^{7}Sr/^{86}Sr)i$	εNd(t)	Reference
Early Cretaceous intrusions (contd.)							
quartz monzodiorite	whole-rock	TLJGS01	Jiguanshan	Shizishan	0.70672	-12.3	(6)
quartz diorite	whole-rock	TLBC02	Baocun	Shizishan	0.70764	-13.5	(6)
quartz monzodiorite	whole-rock	TLSTJ02	Shatanjiao	Shatanjiao	0.70845	-12.7	(6)
diorite porphyry	whole-rock	TLXQT02	Xiaoqingtang	Xinqiao	0.70820	-14.2	(6)
quartz diorite	whole-rock	TLTEBD01	Tianébaodan	Tongguanshan	0.70678	-14.9	(6)
quartz diorite	whole-rock	TLHS01	Hushan	Tongguanshan	0.70915	-16.7	(6)
quartz monzodiorite	whole-rock	TLWLS01	Shizishan	Shizishan	0.70677	-13.6	(6)
quartz diorite	whole-rock	TLFHS01	Fenghuangshan	Fenghuangshan	0.70930	-15.6	(6)
quartz diorite	whole-rock	TGS16	Tongguanshan	Tongguanshan	0.70720	-15.2	(6)
quartz monzodiorite	whole-rock	TLJKL01	Jinkouling	Tongguanshan	0.70688	-14.9	(6)
quartz monzodiorite	whole-rock	TLHC01	Hucun	Shizishan	0.70953	-14.3	(6)
granodiorite	whole-rock	TLQTY01	Qiaotouyang	Shatanjiao	0.70824	-13.6	(6)
Archean mid- to lower crustal basement							
Dongling group	whole-rock	AC-42	N/A	N/A	0.71616	-18.5	(7)
Dongling group	whole-rock	AC-28	N/A	N/A	0.72123	-7.0	(7)
Kongling group	whole-rock	H45	N/A	N/A	0.71834	-43.2	(8)
Kongling group	whole-rock	H44	N/A	N/A	0.71486	-38.5	(8)
Kongling group	whole-rock	H37	N/A	N/A	0.71209	-39.7	(8)
Kongling group	whole-rock	H34	N/A	N/A	0.70724	-38.9	(8)

Abbreviations: apa – apatite; amph – amphibole; plag – plagioclase; N/A – not applicable

References

(1) this study

(2) Tang, Y. *et al. Geology of Copper-Gold Polymetallic Deposits in the Along-Changjiang Area of Anhui Province* (Geological Publishing House, Beijing, 1998). (in Chinese with English abstract)

(3) Du, J., Du, Y. & Cao, Y. Important role of hornblende fractionation in generating the adakitic magmas in Tongling, Eastern china: evidence from amphibole megacryst and cumulate xenoliths and host gabbros. *Int. Geol. Rev.* **60**, 1381-1403 (2018).

(4) Chen, C., Chen, B., Li, Z. & Wang, Z. Important role of magma mixing in generating the Mesozoic monzodioritic–granodioritic intrusions related to Cu mineralization, Tongling, East China: Evidence from petrological and in situ Sr-Hf isotopic data. *Lithos* **248-251**, 80-93 (2016).

(5) Yan, J., Chen, J. & Xu, X. Geochemistry of Cretaceous mafic rocks from the lower Yangtze region, Eastern china: characteristics and evolution of the lithospheric mantle. *J. Asian. Earth. Sci.* **33**, 177-193 (2008).

(6) Xie, J., Yang, X. Sun, W. & Du, J. Early cretaceous dioritic rocks in the Tongling region, Eastern China: Implications for the tectonic settings. *Lithos* **150**, 49-61 (2012b).

(7) Xing, F., Xu, X. & Li, Z. Discovery of early Proterozoic basement in middle to lower Yangtze region and its significance. *Chinese Sci. Bull.* **39**, 135-139 (1994).

(8) Ma, C., Ehlers, C., Xu, C., Li, Z. & Yang, K. The roots of the Dabieshan ultrahigh-pressure metamorphic terrane: constraints from geochemistry and Nd-Sr isotope systematics. *Precambrian Res.* **102**, 279-301 (2000).

Supplementary Table DR4 Electron microprobe analyses of minerals (all values in wt%)

Sample	mineral	SiO_2	TiO_2	Al_2O_3	FeO_{tot}	MnO	MgO	CaO	Na_2O	K_2O	BaO	F	Cl	Total
XTGS-10	cpx	49.8	0.7	4.1	9.1	0.17	11.8	23.2	0.6	0.0	0.00	0.00	0.00	99.5
XTGS-10	cpx	48.3	0.9	5.4	10.7	0.18	10.4	22.7	0.7	0.0	0.00	0.00	0.00	99.4
XTGS-10	cpx	49.1	0.8	4.9	9.3	0.25	11.6	22.5	0.8	0.0	0.08	0.00	0.00	99.3
XTGS-10	cpx	52.2	0.2	1.6	8.7	0.39	12.8	23.4	0.5	0.0	0.00	0.00	0.02	99.8
XTGS-10	cpx	49.5	0.9	4.9	8.9	0.18	11.6	22.7	0.7	0.0	0.00	0.00	0.00	99.4
K6-69	cpx	49.4	1.1	5.1	7.5	0.18	13.6	21.9	0.5	0.0	0.00	0.00	0.00	99.3
K6-69	cpx	50.1	0.8	4.4	6.3	0.14	14.4	22.5	0.4	0.0	0.00	0.00	0.01	99.0
K6-69	cpx	49.3	1.0	5.8	7.1	0.19	13.6	22.4	0.4	0.0	0.00	0.00	0.00	99.7
K6-69	cpx	49.8	0.9	4.9	7.6	0.24	13.7	21.9	0.5	0.0	0.00	0.00	0.00	99.5
K6-69	cpx	50.9	0.7	4.2	6.0	0.06	15.1	22.7	0.4	0.0	0.00	0.00	0.01	100.0
K6-69	cpx	49.9	0.8	4.9	7.4	0.20	13.7	22.1	0.4	0.0	0.00	0.00	0.00	99.6
K6-69	cpx	50.6	0.7	4.0	7.2	0.18	14.3	22.1	0.4	0.0	0.00	0.00	0.00	99.5
K6-69	cpx	48.2	1.1	6.6	8.1	0.24	12.7	21.6	0.6	0.0	0.04	0.00	0.01	99.2
K6-69	cpx	50.8	0.7	4.0	6.5	0.10	14.7	22.3	0.4	0.0	0.09	0.00	0.00	99.6
K6-69	cpx	49.3	1.0	5.8	6.8	0.15	13.7	22.6	0.5	0.0	0.00	0.00	0.00	99.9
K6-69	amph	40.9	2.7	13.7	9.9	0.11	14.0	11.7	2.1	1.8	0.00	0.16	0.01	97.0
K6-69	amph	40.3	2.9	13.9	11.0	0.10	13.5	11.6	2.2	1.8	0.08	0.16	0.02	97.5
K6-69	amph	40.4	2.9	13.8	10.6	0.08	13.8	11.6	2.0	1.8	0.24	0.15	0.01	97.4
K6-69	amph	40.4	2.8	13.8	10.2	0.00	14.0	11.9	2.1	2.0	0.00	0.08	0.00	97.3
K6-69	amph	40.4	2.9	14.0	10.7	0.09	13.6	11.6	1.9	2.0	0.07	0.12	0.00	97.3
K6-69	amph	40.4	2.8	13.9	10.6	0.14	13.6	11.5	2.2	1.9	0.09	0.14	0.01	97.3
K6-69	amph	40.1	2.8	14.0	10.7	0.05	13.6	11.7	2.1	1.8	0.00	0.13	0.01	97.0
K6-69	bio	37.1	3.5	16.7	10.2	0.03	18.3	0.0	0.8	8.8	0.20	0.46	0.00	96.0
K6-69	bio	37.0	3.5	16.5	10.3	0.08	18.2	0.0	0.8	8.9	0.42	0.31	0.01	95.8
K6-69	bio	37.1	3.5	16.6	10.4	0.04	18.1	0.0	0.8	8.7	0.09	0.25	0.01	95.5
K6-69	bio	37.0	3.6	16.4	10.4	0.05	18.1	0.0	0.8	8.9	0.00	0.25	0.01	95.4
K6-69	bio	37.3	3.6	16.6	10.5	0.11	18.2	0.0	0.8	8.8	0.17	0.32	0.01	96.4
K6-69	bio	37.0	3.6	16.4	11.1	0.07	17.6	0.0	0.7	8.9	0.21	0.60	0.01	96.0
K6-69	bio	36.6	3.8	16.0	12.1	0.09	17.3	0.0	0.6	8.9	0.18	0.65	0.03	96.2
K6-69	bio	36.8	3.5	16.4	10.7	0.06	17.8	0.0	0.8	9.0	0.00	0.67	0.01	95.7
K6-45	amph	39.2	2.5	13.9	8.8	0.05	14.4	11.9	1.9	2.0	0.00	0.06	0.01	94.8
K6-45	amph	39.3	2.5	13.9	8.6	0.04	14.4	11.7	2.1	2.0	0.09	0.02	0.00	94.7
K6-45	amph	38.2	2.7	14.1	10.9	0.09	13.1	11.7	1.9	1.9	0.05	0.11	0.02	94.6
K6-68	cpx	49.8	1.1	4.5	8.1	0.32	13.9	21.2	0.6	0.0	0.00	0.00	0.00	99.5
K6-68	cpx	50.2	1.0	4.5	8.4	0.35	14.0	20.6	0.6	0.0	0.01	0.00	0.00	99.5
K6-68	cpx	50.4	0.9	3.9	7.4	0.19	14.3	21.4	0.5	0.0	0.00	0.00	0.01	99.1
K6-68	cpx	49.5	1.2	4.7	8.2	0.26	13.7	21.4	0.5	0.0	0.00	0.00	0.00	99.5
K6-68	cpx	50.1	1.1	4.3	7.7	0.25	14.3	20.9	0.5	0.0	0.00	0.00	0.01	99.2
K6-68	cpx	50.3	1.0	3.8	7.3	0.17	14.5	21.6	0.4	0.0	0.00	0.00	0.01	99.1
K6-68	bio	35.4	4.2	13.7	14.3	0.32	15.4	0.0	0.3	9.1	0.73	0.74	0.11	94.1
K6-68	bio	36.6	5.8	13.9	15.0	0.31	14.3	0.0	0.4	9.0	0.58	0.58	0.07	96.6
K6-68	bio	36.4	5.9	14.0	14.7	0.35	14.5	0.0	0.4	9.0	0.06	0.63	0.06	95.9
K6-68	bio	36.5	4.5	14.8	13.5	0.23	15.8	0.0	0.6	8.7	0.03	0.69	0.04	95.3
K6-68	bio	35.2	4.7	13.6	14.0	0.33	15.2	0.0	0.4	8.8	0.63	0.79	0.07	93.7
K6-68	bio	35.9	5.0	14.5	14.0	0.25	15.0	0.0	0.6	8.7	0.69	0.61	0.04	95.4

Supplementary Table DR4 (contd.)

Sample	mineral	SiO_2	TiO_2	Al_2O_3	FeO_{tot}	MnO	MgO	CaO	Na_2O	K_2O	BaO	F	Cl	Total
JC027	cpx	52.1	0.4	3.1	6.2	0.20	15.8	21.5	0.4	0.0	0.09	0.00	0.00	99.7
JC027	cpx	49.9	0.9	6.0	6.2	0.14	14.4	22.3	0.4	0.0	0.00	0.00	0.00	100.2
JC027	cpx	48.4	1.2	6.9	5.9	0.11	13.9	22.3	0.4	0.0	0.09	0.00	0.02	99.2
JC027	cpx	48.4	1.0	6.7	8.2	0.20	12.8	22.1	0.6	0.0	0.18	0.00	0.00	100.2
JC027	cpx	49.2	1.0	6.0	6.5	0.13	14.1	22.0	0.5	0.0	0.04	0.00	0.01	99.4
JC027	cpx	49.2	1.0	6.3	6.1	0.11	14.4	22.3	0.4	0.0	0.25	0.00	0.00	100.1
JC027	cpx	49.2	0.9	5.9	6.8	0.18	14.1	22.1	0.5	0.0	0.08	0.00	0.02	99.8
JC027	amph	39.7	3.0	14.4	10.8	0.07	13.7	11.5	2.1	1.8	0.42	0.13	0.01	97.6
JC027	amph	39.5	3.0	14.2	12.7	0.15	12.2	11.6	2.4	1.6	0.20	0.00	0.03	97.5
JC027	amph	38.8	2.8	15.0	13.0	0.14	12.0	11.6	2.3	1.5	0.24	0.01	0.01	97.4
JC027	amph	40.5	3.1	14.0	10.6	0.12	13.7	11.4	2.2	1.6	0.04	0.11	0.01	97.3
JC027	amph	39.1	2.7	14.9	12.2	0.11	12.4	11.7	2.2	1.6	0.00	0.08	0.02	96.9
JC027	amph	40.4	2.7	14.2	9.2	0.13	14.5	11.8	2.0	1.9	0.00	0.16	0.01	96.9
JC027	amph	38.7	2.9	15.4	11.7	0.13	12.6	11.8	2.0	1.9	0.03	0.01	0.01	97.1
JC027	amph	39.2	2.8	14.9	12.4	0.16	12.5	11.6	2.2	1.6	0.17	0.00	0.01	97.4
JC027	amph	39.0	2.8	15.0	13.1	0.18	11.7	11.6	2.3	1.5	0.00	0.06	0.01	97.2
JC027	amph	38.9	2.8	15.0	12.6	0.11	12.1	11.7	2.1	1.6	0.04	0.08	0.01	97.0
zk207-1	cpx	49.7	0.9	4.4	8.4	0.23	13.0	22.7	0.5	0.0	0.04	0.00	0.00	99.7
zk207-1	cpx	49.0	1.0	4.9	8.4	0.14	12.6	22.8	0.5	0.0	0.00	0.00	0.00	99.4
zk207-1	cpx	49.6	0.8	4.3	8.3	0.28	12.9	22.7	0.5	0.0	0.00	0.00	0.00	99.4
zk207-1	cpx	50.7	0.7	3.5	8.1	0.14	13.4	22.9	0.5	0.0	0.00	0.00	0.00	100.0
zk207-1	cpx	49.3	1.0	5.0	8.7	0.23	12.5	22.7	0.6	0.0	0.00	0.00	0.00	100.0
zk207-1	cpx	49.5	0.9	4.7	8.6	0.20	12.5	22.9	0.5	0.0	0.04	0.00	0.01	99.8
zk207-1	amph	40.6	2.7	13.3	12.2	0.20	12.6	11.8	2.5	1.2	0.00	0.02	0.10	97.1
zk207-1	amph	40.5	2.9	13.4	12.8	0.18	12.5	11.8	2.4	1.2	0.00	0.01	0.04	97.8
zk207-1	amph	40.3	2.9	13.6	13.5	0.15	12.1	11.7	2.6	1.1	0.00	0.00	0.01	97.7
zk207-1	amph	40.3	2.9	13.3	12.9	0.17	12.5	11.7	2.6	1.1	0.29	0.00	0.03	97.7
zk207-1	amph	41.1	2.8	12.8	12.8	0.17	12.8	11.6	2.5	1.0	0.37	0.02	0.02	97.9
zk207-1	amph	39.8	2.9	14.6	11.1	0.06	13.5	11.7	2.0	1.7	0.00	0.04	0.01	97.4
zk207-1	amph	39.7	3.0	14.4	10.7	0.05	13.4	11.8	2.1	1.7	0.00	0.10	0.01	96.9
zk207-10	cpx	48.9	1.0	5.0	9.3	0.20	12.1	22.8	0.5	0.0	0.00	0.00	0.01	99.9
zk207-10	cpx	48.0	1.3	6.4	9.7	0.20	11.9	22.9	0.5	0.0	0.00	0.00	0.01	100.9
zk207-10	cpx	47.6	1.4	6.6	9.0	0.17	11.6	22.7	0.5	0.0	0.38	0.00	0.00	100.0
zk207-10	cpx	47.3	1.3	6.6	9.1	0.18	11.6	22.6	0.5	0.0	0.29	0.00	0.01	99.5
zk207-10	cpx	46.4	1.6	7.8	9.5	0.21	11.1	22.9	0.5	0.0	0.00	0.00	0.01	100.1
zk207-10	amph	39.7	2.8	14.5	12.4	0.06	12.3	12.1	2.4	1.1	0.54	0.15	0.02	98.2
zk207-10	amph	39.9	2.9	14.2	13.3	0.18	11.9	11.8	2.6	1.1	0.25	0.13	0.03	98.2
zk207-10	amph	39.7	2.9	14.6	12.9	0.15	12.2	11.9	2.5	1.1	0.03	0.00	0.03	97.9
zk207-10	amph	39.5	2.9	14.5	13.9	0.20	11.4	11.8	2.8	1.1	0.25	0.10	0.01	98.4
zk207-10	amph	39.4	2.8	14.7	13.0	0.22	12.2	12.0	2.3	1.2	0.12	0.07	0.01	97.9
zk207-14	cpx	50.1	1.2	4.9	8.4	0.11	12.7	22.8	0.2	0.0	0.27	0.00	0.00	100.7
zk207-14	amph	41.0	2.8	13.9	12.6	0.15	11.7	11.7	2.9	1.3	0.14	0.21	0.03	98.5
zk207-14	amph	40.3	3.7	13.8	13.4	0.15	11.1	11.8	2.6	1.3	0.10	0.27	0.02	98.5
zk207-14	amph	40.7	3.0	14.5	12.3	0.09	11.6	11.8	2.9	1.3	0.26	0.26	0.04	98.6
zk207-14	amph	40.6	3.0	14.2	12.3	0.18	11.8	11.9	2.9	1.2	0.00	0.43	0.03	98.5
zk207-14	amph	41.0	3.2	13.0	14.1	0.14	11.2	11.4	3.0	1.3	0.09	0.31	0.10	98.7
zk207-14	amph	40.9	2.8	14.2	12.1	0.16	11.8	11.6	2.9	1.2	0.25	0.33	0.04	98.2

Supplementary Table DR4 (contd.)

Sample	mineral	SiO_2	TiO_2	Al_2O_3	FeO_{tot}	MnO	MgO	CaO	Na_2O	K_2O	BaO	F	Cl	Total
CS-35	cpx	49.7	1.0	4.8	7.3	0.14	13.8	22.8	0.3	0.0	0.13	0.00	0.01	100.0
CS-35	cpx	49.7	1.0	4.1	6.8	0.15	14.4	23.2	0.3	0.0	0.33	0.00	0.01	100.0
CS-35	cpx	50.0	0.9	4.1	7.2	0.15	13.9	23.0	0.3	0.0	0.00	0.00	0.00	99.6
CS-35	amph	40.4	2.6	13.3	11.0	0.08	14.3	12.1	2.1	1.5	0.04	0.03	0.01	97.5
CS-35	amph	41.2	2.6	13.0	11.0	0.02	14.1	12.0	2.3	1.4	0.31	0.65	0.03	98.6
CS-35	amph	40.6	2.6	13.1	11.3	0.14	13.8	11.9	2.5	1.4	0.20	0.84	0.01	98.4
CS-35	amph	40.2	2.6	13.4	11.2	0.07	14.0	11.9	2.2	1.4	0.00	0.07	0.02	97.1
CS-h1	amph	41.1	2.5	13.2	11.7	0.20	13.6	11.7	2.2	1.1	0.16	0.02	0.01	97.6
CS-h1	amph	41.0	2.6	13.2	11.8	0.13	13.6	11.8	2.1	1.1	0.16	0.00	0.03	97.5
CS-h1	amph	41.0	2.6	13.3	12.0	0.21	13.5	11.8	2.2	1.1	0.20	0.04	0.02	98.0
CS-24	cpx	50.2	0.7	3.3	6.9	0.19	14.7	22.9	0.3	0.0	0.10	0.00	0.00	99.4
CS-24	cpx	49.7	0.9	4.5	7.2	0.12	14.1	23.1	0.3	0.0	0.29	0.00	0.00	100.1
CS-24	cpx	49.7	0.9	4.4	6.8	0.19	14.2	23.1	0.3	0.0	0.04	0.00	0.00	99.6
CS-24	amph	40.7	2.4	13.0	10.4	0.12	14.8	12.2	2.2	1.5	0.23	0.56	0.01	98.0
CS-24	amph	40.9	2.4	13.1	10.4	0.12	14.7	12.0	2.2	1.6	0.36	0.00	0.02	97.8
CS-35 host	cpx	51.6	0.7	2.3	7.3	0.50	14.3	22.2	0.4	0.0	0.00	0.00	0.00	99.2
CS-35 host	cpx	51.8	0.5	2.4	8.5	0.52	13.3	22.0	0.6	0.0	0.00	0.00	0.00	99.5
CS-35 host	cpx	52.1	0.4	1.6	8.3	0.77	14.1	21.3	0.5	0.0	0.08	0.00	0.00	99.2
CS-35 host	cpx	51.5	0.5	1.9	7.7	0.35	13.8	22.7	0.6	0.0	0.21	0.00	0.01	99.3
CS-35 host	amph	41.4	2.2	12.4	10.1	0.17	14.6	11.7	2.3	1.5	0.03	1.03	0.01	97.4
CS-35 host	amph	39.9	2.7	13.3	14.5	0.19	11.3	11.5	2.5	1.4	0.09	0.68	0.03	98.0
CS-35 host	bio	36.7	5.1	13.6	16.6	0.23	13.3	0.0	0.2	9.3	0.00	0.52	0.12	95.6
CS-35 host	bio	36.4	4.3	13.7	16.2	0.29	14.0	0.0	0.1	9.4	0.00	0.63	0.15	95.2
CS-35 host	bio	36.4	4.1	13.9	15.1	0.30	14.2	0.0	0.1	9.1	0.04	0.66	0.16	93.9
CS01	cpx	47.4	1.3	5.9	9.2	0.24	12.1	22.7	0.4	0.0	0.07	0.00	0.00	99.2
CS01	cpx	45.8	1.6	7.4	10.0	0.17	11.0	22.5	0.6	0.0	0.00	0.00	0.01	99.1
CS01	cpx	48.3	1.2	5.6	8.5	0.19	12.6	22.8	0.4	0.0	0.03	0.00	0.01	99.6
CS01	cpx	47.4	1.3	6.2	9.0	0.25	12.1	22.7	0.4	0.0	0.04	0.00	0.01	99.4
CS01	cpx	47.9	1.3	6.1	9.1	0.17	12.0	22.7	0.5	0.0	0.08	0.00	0.00	99.8
CS01	cpx	48.0	1.2	6.0	8.3	0.21	12.7	23.0	0.4	0.0	0.00	0.00	0.00	99.8
CS01	amph	40.6	2.8	13.5	12.0	0.18	13.1	11.9	2.4	1.1	0.02	0.33	0.01	98.0
CS01	amph	40.2	2.9	13.9	11.5	0.21	13.0	12.1	2.6	1.2	0.00	0.12	0.01	97.7
CS01	amph	40.1	2.8	13.7	11.9	0.14	13.0	12.0	2.5	1.1	0.09	0.48	0.03	97.8
CS01	amph	39.9	2.9	13.5	12.3	0.18	12.9	11.7	2.4	1.1	0.15	0.39	0.03	97.4
CS01	amph	40.3	2.9	13.4	12.4	0.13	12.7	11.8	2.5	1.2	0.06	0.75	0.02	98.2
CS01	phlog	35.8	4.5	14.8	16.2	0.25	13.3	0.0	0.2	9.0	0.22	0.89	0.11	95.2

Abbreviations: amph – amphibole; cpx – clinopyroxene; bio – biotite; phlog – phlogopite

Supplementary Table DR5 LA-ICP-MS analyses of entire, unexposed sulfide inclusions

Sample	Host	Type	Size (µm	S (wt%)	Mn (wt%)	Fe (wt%)	Co (wt%)	Ni (wt%)	Cu (wt%)	As (ppm)	Se (ppm)	Mo (ppm)
K6-69	amph	SL	20	37.4	0.05	43.1	0.15	1.24	18.0	<4.6	163	<2.8
K6-69	amph	MSS	50	39.5	0.01	55.1	0.27	0.92	4.3	<0.8	85	0.9
K6-69	amph	MSS	50	40.3	0.04	54.7	0.25	0.83	3.9	<0.8	63	0.9
K6-69	amph	MSS	50	41.6	0.05	52.8	0.26	0.75	4.6	<0.3	70	0.7
K6-69	amph	MSS	45	41.3	0.03	54.5	0.12	0.47	3.6	<0.4	71	0.5
K6-69	amph	MSS	40	40.0	0.05	55.4	0.22	0.83	3.5	<0.7	81	0.7
K6-69	cpx	MSS	20	39.1	0.08	56.4	0.20	0.71	3.6	<2.4	72	1.4
K6-69	cpx	MSS	35	41.1	0.04	54.5	0.16	0.68	3.6	<0.9	79	0.8
K6-69	cpx	MSS	25	42.1	0.01	52.9	0.22	0.79	3.9	<2.4	88	<1.6
K6-69	cpx	MSS	20	42.0	0.08	50.9	0.29	1.02	5.8	<1.6	92	<1.0
K6-69	cpx	MSS	20	41.6	0.03	52.6	0.30	1.13	4.4	<2.4	83	<1.6
K6-69	cpx	MSS	35	40.8	0.03	54.4	0.25	0.88	3.7	<0.4	75	1.0
K6-45	amph	MSS	27	40.4	0.07	54.2	0.19	1.28	4.0	<2.8	67	<1.3
K6-45	amph	MSS	30	42.3	0.07	53.5	0.08	0.72	3.4	<2.1	72	<1.0
K6-45	amph	MSS	40	43.7	0.02	52.1	0.22	1.04	3.0	<1.2	81	<1.2
K6-45	amph	MSS	40	40.1	0.06	54.4	0.26	1.18	4.1	<0.7	69	0.8
K6-45	amph	MSS	40	41.0	0.04	54.3	0.21	1.02	3.5	<0.7	71	0.9
K6-45	amph	MSS	40	40.1	<0.05	55.3	0.03	0.44	4.1	<0.6	69	<0.6
K6-45	amph	MSS	37	40.7	0.03	54.2	0.19	1.03	3.9	<0.6	66	0.9
K6-45	amph	MSS	50	40.7	0.05	52.6	0.31	1.34	5.0	3.9	64	1.3
K6-68	cpx	MSS	23	40.5	0.12	57.1	0.18	0.17	2.0	<1.5	45	1.1
K6-68	cpx	MSS	23	39.3	0.08	55.7	0.18	0.54	4.2	<2.4	58	2.0
JC027	amph	MSS	29	42.5	0.05	55.6	0.19	0.20	1.5	<4.6	38	<2.5
JC027	amph	MSS	5	42.7	0.06	54.7	0.18	0.24	2.2	<63	<470	<39
JC027	amph	MSS	20	42.5	0.01	54.4	0.21	0.66	2.3	<13	59	<8.1
JC027	amph	MSS	17	41.0	0.10	57.8	0.05	0.13	0.9	<20	<150	<13
JC027	amph	MSS	18	39.1	0.07	59.1	0.16	0.36	1.1	<21	<160	<8.5
ZK207-14	amph	MSS	25	41.7	0.01	56.7	0.17	0.05	1.4	2.5	47	2.3
ZK207-14	amph	MSS	30	42.7	0.04	55.2	0.21	0.07	1.8	2.9	41	1.2
ZK207-14	amph	MSS	27	40.3	<0.05	58.5	0.15	0.02	1.0	5.4	33	9.2
ZK207-14	amph	MSS	18	41.1	0.03	57.2	0.19	0.04	1.5	<2.3	50	10.7
ZK207-14	amph	MSS	27	42.3	0.01	56.1	0.16	0.03	1.4	2.2	44	<1.1
ZK207-14	amph	MSS	18	41.7	0.05	55.8	0.16	0.15	2.3	<2.2	41	4.9
ZK207-14	amph	MSS	30	42.2	0.03	55.4	0.27	0.20	1.9	1.4	54	<1.1
CS-h1	amph	MSS	13	36.4	0.20	62.1	0.13	0.09	1.1	<21	54	<13

Abbreviations: amph – amphibole; cpx – clinopyroxene; SL – sulfide liquid; MSS – monosulfide solid solution

Supplementary Table DR5 (contd.)

Sample	Host	Type	Size (µm	Pd[1] (ppm)	Ag (ppm)	Cd (ppm)	Te (ppm)	Pt (ppm)	Au (ppm)	Tl (ppm)	Pb (ppm)	Bi (ppm)
K6-69	amph	SL	20	7.8	130.5	11.7	37.8	5.7	3.5	8.7	675.1	172.9
K6-69	amph	MSS	50	6.3	2.0	<1.2	1.6	1.3	0.1	0.1	1.5	0.6
K6-69	amph	MSS	50	3.6	3.3	<1.7	1.2	5.5	0.1	<0.0	2.3	0.7
K6-69	amph	MSS	50	2.2	2.7	1.5	1.4	0.6	0.0	<0.1	1.1	0.3
K6-69	amph	MSS	45	3.1	1.9	1.0	1.3	1.8	0.2	<0.0	1.2	0.4
K6-69	amph	MSS	40	3.1	3.2	<0.9	1.5	0.7	0.2	<0.1	1.5	0.6
K6-69	cpx	MSS	20	4.0	2.9	<5.3	<2.8	2.5	<0.4	<0.2	3.2	2.0
K6-69	cpx	MSS	35	1.9	2.1	<1.6	<1.4	0.8	<0.1	<0.1	1.9	0.2
K6-69	cpx	MSS	25	3.3	3.5	<3.5	<4.0	4.8	<0.2	<0.2	4.1	2.4
K6-69	cpx	MSS	20	2.7	4.2	3.2	<2.6	3.5	0.1	<0.1	9.9	1.1
K6-69	cpx	MSS	20	2.6	3.0	<3.5	<4.0	3.2	<0.2	<0.2	2.3	<.03
K6-69	cpx	MSS	35	2.6	2.0	1.4	1.1	2.1	<0.2	<0.1	2.0	0.4
K6-45	amph	MSS	27	4.3	2.5	<3.5	<3.0	1.7	<0.2	<0.2	1.9	0.6
K6-45	amph	MSS	30	4.7	2.3	<2.6	<2.2	2.2	<0.2	<0.1	1.3	<0.3
K6-45	amph	MSS	40	2.0	2.5	<2.6	<2.1	0.7	<0.2	<0.3	1.3	0.4
K6-45	amph	MSS	40	3.0	2.2	<1.5	2.3	0.8	<0.1	<0.2	1.5	0.2
K6-45	amph	MSS	40	2.2	2.6	<1.5	<1.3	0.6	<0.1	<0.2	1.1	0.3
K6-45	amph	MSS	40	1.7	1.3	3.5	2.1	<0.1	<0.1	0.2	2.7	1.7
K6-45	amph	MSS	37	1.2	19.0	6.4	3.1	1.0	0.2	0.1	2.3	3.5
K6-45	amph	MSS	50	2.6	3.0	1.9	1.4	1.0	0.1	1.8	3.5	0.3
K6-68	cpx	MSS	23	1.2	3.4	2.6	3.2	<0.6	<0.3	<0.1	3.0	0.7
K6-68	cpx	MSS	23	3.7	3.3	4.5	<2.8	<1.7	<0.3	0.3	1.9	0.3
JC027	amph	MSS	29	0.8	2.7	<7.2	0.6	<0.7	<0.6	<0.3	1.7	0.9
JC027	amph	MSS	5	<67	<27	<90	<115	<17	<4.7	<8.8	<247	<10
JC027	amph	MSS	20	1.6	1.7	<23	<24	<3.5	<1.0	<1.9	<5.7	<2.2
JC027	amph	MSS	17	<21	<9.0	<37	<37	<5.5	<1.5	<2.9	3.9	<3.4
JC027	amph	MSS	18	<7.7	<6.8	<20	<19	<2.5	<2.0	<1.3	<5.0	<3.1
ZK207-14	amph	MSS	25	<1.1	2.4	<3.0	<6.1	<0.3	<0.2	<0.2	2.0	0.5
ZK207-14	amph	MSS	30	<1.2	6.2	<4.3	<1.6	<0.3	0.8	0.3	55.8	1.5
ZK207-14	amph	MSS	27	<1.1	2.8	3.3	3.3	<0.3	<0.2	<0.1	1.2	1.1
ZK207-14	amph	MSS	18	1.3	6.7	<6.2	4.1	<0.4	0.6	0.6	99.0	1.2
ZK207-14	amph	MSS	27	<1.4	2.1	<4.3	3.6	<0.3	<0.2	<0.2	6.0	0.7
ZK207-14	amph	MSS	18	1.4	3.2	<3.7	<2.2	<0.5	<0.3	<0.1	0.7	0.2
ZK207-14	amph	MSS	30	1.3	18.5	8.1	1.6	<0.3	0.9	<0.1	27.2	4.2
CS-h1	amph	MSS	13	<8.6	6.2	<23	<47	<3.8	<1.6	<0.7	1.4	<1.9

[1] Corrected for $^{65}Cu^{40}Ar$ interference using the equation: $Pd_{excess}(ppm) = 0.4063 * Cu(wt\%) - 1.27$ (Chang and Audétat, 2018)

Supplementary Table DR6 Sample coordinates

Sample	Easting	Northing
XTGS-10	117°48′34"	30°54′21"
K6-69	117°50'04"	30°52'29"
K6-45	117° 50' 04"	30° 52' 29"
K6-68	117° 50' 04"	30° 52' 29"
JC027	117°50′41"	30°52′18"
ZK207-1	117°53′54"	30°54′47"
ZK207-10	117°53′54"	30°54′47"
ZK207-14	117°53′54"	30°54′47"
CS-35	117°53′32"	30°55′16"
CS-h1	117°53′32"	30°55′16"
CS-24	117°53′32"	30°55′16"
CS-35	117°53′32"	30°55′16"
CS01	117°52′40"	30°54′30"

4. Supplementary References

Audétat, A., 2010, Source and evolution of molybdenum in the porphyry-Mo(-Nb) deposit at Cave Peak, Texas: Journal of Petrology, v. 51, p. 1739-1760.

Audétat. A., 2015, Compositional evolution and formation conditions of magmas and fluids related to porphyry Mo mineralization at Climax, Colorado: Journal of Petrology, v. 56, p. 1519-1546.

Brenan, J. M., 2015, Se–Te fractionation by sulfide–silicate melt partitioning: Implications for the composition of mantle-derived magmas and their melting residues: Earth Planetary Science Letters, v. 422, p. 45-57.

Danyushevsky, L. V., Della-Pasqua, F. N., and Sokolov, S., 2000, Re-equilibration of melt inclusions trapped by magnesian olivine phenocrysts from subduction-related magmatism: petrological implications: Contributions to Mineralogy and Petrology, v. 138, p. 68-83.

Du, Y., Qin, X., and Tian, S., 2004, Mesozoic magmatic to hydrothermal process in the Tongguanshan ore field, Tongling, Anhui province, China: evidence from xenoliths and their hosts: Acta Petrologica Sinica, v. 20, p. 339-350 (in Chinese with English abstract).

Fortin, M.-A., Riddle, J., Desjardins-Langlais, Y., and Baker, D. R., 2015, The effect of water on the sulfur concentration at sulfide saturation (SCSS) in natural melts: Geochimica et Cosmochimica Acta, v. 160, p. 100-116.

Gale, A., Dalton, C. A., Langmuir, C. H., Su, Y., and Schilling, J.-G., 2013, The mean composition of ocean ridge basalts: Geochemistry Geophysics Geosystems, v. 14, p. doi:10.1029/2012GC004334.

Grondahl, C., and Zajacz, Z., 2017, Magmatic controls on the genesis of porphyry Cu–Mo–Au deposits: The Bingham Canyon example: Earth and Planetary Science Letters, v. 480, p. 53-65.

Guo, H., Lu, J., Jiang, S., Zhang, R., and Zhao, Z., 2013, Chronology, Hf isotopes, geochemistry, and petrogenesis of the magmatic rocks in the Shizishan ore field of Tongling, Anhui province.: Science China Earth Sciences, v. 56, p. 993-1013.

Halter, W. E., Pettke, T., and Heinrich, C. A., 2004a, Laser-ablation ICP-MS analysis of silicate melt and sulfide melt inclusions in an andesitic complex I: analytical approach and data evaluation: Contributions to Mineralogy and Petrology, v. 147, p. 385-396.

Huang, S., Xu, Z., and Gu, L., 2004, A discussion on geochemical characteristics and genesis of intrusions in Shizishan orefield, Tongling area, Anhui Province: Geological Journal of China Universities, v. 10, p. 217-226.

Huang, Y., Chubakov, V., Mantovani, F., Rudnick, R. L., and McDonough, W. F., 2013, A reference Earth model for the heat-producing elements and associated geoneutrino flux: Geochemistry Geophysics Geosystems, v. 14, p. doi:10.1002/ggge.20129.

Jochum, K. P., Weis, D., Stoll, B., Kuzmin, D., Yang, Q., Raczek, I., Jacob, D. E., Stracke, A., Birbaum, K., Frick, D. A., Günther, D., and Enzweiler, J., 2011, Determination of reference values for NIST SRM 610-617 glasses following ISO guidelines: Geostandards and Geoanalytical Research, v. 35, p. 397-429.

Jugo, P. J., Wilke, M., and Botcharnikov, R. E., 2010, Sulfur K-edge XANES analysis of natural and synthetic basaltic glasses: implications for S speciation and S content as function of oxygen fugacity: Geochimica et Cosmochimica Acta, v. 74, p. 5926-5938.

Kay, S. M., Jicha, B. R., Citron, G. L., Kay, R. W., Tibbetts, A. K., and Rivera, T. A., 2019, The calc-alkaline Hidden Bay and Kagalaska plutons and the construction of the central Aleutian oceanic arc crust: Journal of Petrology, v. 60, p. 393-439.

Leake, B. E., and others, a., 1997, Nomenclature of amphiboles: report of the subcommittee on amphiboles of the international mineralogical association, commission on new minerals and mineral names: Canadian Mineralogist, v. 35, p. 219-246.

Li, S., Yang, X., Huang, Y., and Sun, W., 2014, Petrogenesis and mineralization of the Fenghuangshan skarn Cu–Au deposit, Tongling ore cluster field, Lower Yangtze metallogenic Belt: Ore Geology Reviews, v. 58, p. 148-162.

Li, Y., and Audétat, A., 2015, Effects of temperature, silicate melt composition, and oxygen fugacity on the partitioning of V, Mn, Co, Ni, Cu, Zn, As, Mo, Ag, Sn, Sb, W, Au, Pb, and Bi between sulfide phases and silicate melt: Geochimica et Cosmochimica Acta, v. 162, p. 25-45.

Ma, C., Ehlers, C., Xu, C., Li, Z., and Yang, K., 2000, The roots of the Dabieshan ultrahigh-pressure metamorphic terrane: constraints from geochemistry and Nd–Sr isotope systematics: Precambrian Research, v. 102, p. 279-301.

Pettke, T., 2006, In-situ Laser-Ablation-ICP-MS chemical analysis of melt inclusion and prospects for constraining subduction zone magmas, *in* Webster, J. D., ed., Melt inclusions in plutonic rocks, Mineralogical Association of Canada, Short Course Series, Montreal, v. 36, p. 51-80.

Putirka, K. D., 2008, Thermometers and barometers for volcanic systems, *in* Putirka, K. D., and Tepley, F. J. I., eds., Minerals, inclusions and volcanic processes, Reviews in Mineralogy and Geochemistry, Mineralogical Society of America, Chantilly, VA, v. 69, p. 61-120.

Qin, X., 2007, Studies on sulfide-metal oxide inclusions from Mesozoic intrusions and their rock xenoliths in Tongling, Anhui Province [Ph.D. thesis]: China University of Geosciences in Beijing (in Chinese with English abstract).

Ramos, F. C., Wolff, J. A., and Tollstrup, D. L., 2004, Measuring 87Sr/86Sr variation in minerals and groundmass from basalts using LA-MC-ICPMS: Chemical Geology, v. 211, p. 135-158.

Rottier, B., and Audétat, A., 2019, In-situ quantification of chlorine and sulfur in glasses, minerals and melt inclusions by LA-ICP-MS: Chemical Geology, v. 504, p. 1-13.

Sturm, R., 2002, PX-NOMF an interactive spreadsheet program for the computation of pyroxene analyses derived from the electron microprobe: Computers and Geosciences., v. 28, p. 473-483.

Tang, Y. et. al., 1998, Geology of Copper-Gold Polymetallic Deposits in the Along-Changjiang Area of Anhui Province, Geological Publishing House, Beijing, 351 p.

Wang, Q., Xu, J., Zhao, Z., Xiong, X., and Bao, Z., 2003, Petrogenesis of the Mesozoic intrusive rocks in the Tongling area, Anhui Province, China and their constraint on geodynamic process: Science in China Series D: Earth Sciences, v. 46, p. 801-815.

Wang, S., Zhou, T., Yuan, F., Cooke, D. R., Zhang, L., Fu, B., and White, N. C., 2016, Geochemical characteristics of the Shujiadian Cu deposit related intrusion in Tongling: Petrogenesis and implications for the formation of porphyry Cu systems in the Middle-Lower Yangtze River Valley metallogenic belt, Eastern China: Lithos, v. 252-253, p. 185-199.

Wang, S., Zhou, T., Yuan, F., Fan, Y., Zhang, L., and Song, Y., 2015, Petrogenesis of Dongguashan skarn-porphyry Cu–Au deposit related intrusion in the Tongling district, eastern China: Geochronological, mineralogical, geochemical and Hf isotopic evidence: Ore Geology Reviews, v. 64, p. 53-70.

Wu, C., Dong, S., Wu, D., Zhang, X., and Ernst, W., 2017, Late Mesozoic high-K calc-alkaline magmatism in Southeast China: the Tongling example.: International Geology Review, v. 60, p. 1-13.

Wu, C., Gao, Q., Guo, H., Guo, X., Liu, L., Gao, Y., Lei, M., and Qin, H., 2010, Petrogenesis of the intermediate-acid intrusive rocks and zircon SHRIMP dating in Tongling, Anhui, China: Acta Petrologica Sinica, v. 26, p. 2630-2652.

Wu, C., Wang, Z., Qiao, D., Li, H., Hao, M., and Shi, R., 2000, Types of enclaves and their features and origins in intermediate-acid intrusive rocks from the Tongling district, Anhui Province, China: Acta Geological Sinica, v. 74, p. 54-67.

Xie, J., Chen, S., Sun, W., and Yang, X., 2012a, Geochemistry of Early Cretaceous adakitic rocks in Tongling region of Anhui Province: Constraints for rock- and ore-forming: Acta Petrologica Sinica, v. 28, p. 3181-3196.

Xie, J., Yang, X., Sun, W., and Du, J., 2012b, Early Cretaceous dioritic rocks in the Tongling region, eastern China: Implications for the tectonic settings: Lithos, v. 150, p. 49-61.

Xing, F.-M., and Xu, X., 1994, Discovery of the Early Proterozoic basement in the middle-lower reaches of Yangtze river and its significance: Chinese Science Bulletin, v. 39, p. 135-139.

Xu, X., Fan, Q., O'Reilly, S., Jiang, S., Griffin, W. L., Wang, R., and Qiu, J., 2004, U-Pb dating of zircons from quartz diorite and its enclaves at Tongguanshan in Anhui and its petrogenetic implication: Chinese Science Bulletin, v. 49, p. 2073-2082.

Yan, J., Chen, J., and Xu, X., 2008, Geochemistry of Cretaceous mafic rocks from the Lower Yangtze region, eastern China: Characteristics and evolution of the lithospheric mantle: Journal of Asian Earth Sciences, v. 33, p. 177-193.

Yang, Y., Sun, J., Xie, L., Fan, H., and Wu, F., 2008, In situ Nd isotopic measurement of natural geological materials by LA-MC-ICPMS: Chinese Science Bulletin, v. 53, p. 1062-1070.

Yang, Y., Wu, F., Yang, J., Chew, D., Xie, L., Chu, Z., Zhang, Y., and Huang, c., 2014, Sr and Nd isotopic compositions of apatite reference materials used in U–Th–Pb geochronology: Chemical Geology, v. 385, p. 35-55.

Zhang, D., and Audétat, A., 2017, Chemistry, mineralogy and crystallization conditions of porphyry Mo-forming magmas at Urad–Henderson and Silver Creek, Colorado, USA: Journal of Petrology, v. 58, p. 277-296.